



Sulfur-vacancy rich nonstoichiometric $\text{TiS}_{2-x}/\text{NiS}$ heterostructures for superior universal hydrogen evolution

Jing Wu^a, Wenda Zhong^a, Chenfan Yang^a, Wenli Xu^b, Rong Zhao^b, Hui Xiang^b, Qin Zhang^{b,*}, Xuanke Li^{a,b,**}, Nianjun Yang^{c,*}

^a Hunan Province Key Laboratory for Advanced Carbon Materials and Applied Technology, College of Materials Science and Engineering, Hunan University, Changsha 410082, China

^b Hubei Province Key Laboratory of Coal Conversion and New Carbon Materials, School of Chemistry and Chemical Engineering, Wuhan University of Science and Technology, Wuhan 430081, China

^c Institute of Materials Engineering, University of Siegen, Siegen 57076, Germany



ARTICLE INFO

Keywords:

Hydrogen evolution reaction
Nonstoichiometric effect
Sulfur vacancies
d-band center
Electronic structure

ABSTRACT

Water electrolysis has been recognized as one of the most promising approaches to produce green hydrogen and eventually target carbon neutrality. Various cost-effective and light transition metal sulfides have been developed as the electrocatalysts to promote hydrogen evolution reaction (HER), one half-reaction of water electrolysis. Unfortunately, full use of their intrinsic electrocatalytic traits and exposed active sites is still challenging. Here, a nonstoichiometric titanium sulfide/nickel sulfide ($\text{TiS}_{2-x}/\text{NiS}$) hetero-catalyst is designed and constructed to induce a high-density of sulfur vacancies. As a HER electrocatalyst, it features the overpotentials of only 63 and 134 mV at a current density of 10 mA cm^{-2} in 1.0 M KOH and 0.5 M H_2SO_4 , respectively, which is equipped with glorious durability even at high current densities (e.g., 100 mA cm^{-2} and 500 mA cm^{-2}). Such outstanding performance partially stems from the sulfur vacancies induced by a nonstoichiometric effect, namely the intensified interfacial charge transfer nearby the $\text{TiS}_{2-x}/\text{NiS}$ heterointerface. The existence of sulfur vacancies partially regulates the *d*-electronic structure of Ti and Ni active sites, ultimately bringing in reduced energy barrier of water dissociation as well as optimized adsorption free energy for H^* intermediates. The strategy of employing both a nonstoichiometric effect and interface engineering of a metal sulfide catalyst paves a new way to design high-performance and cost-effective HER electrocatalyst in universal media.

1. Introduction

Zero emission of greenhouse gases is indispensable to create a future low carbon energy economy [1]. Clean hydrogen generated from water electrolysis is expected to be one of the effective ways to achieve carbon neutrality by 2050 [2]. The International Energy Agency expects that around 2030 hydrogen produced by water electrolysis, namely hydrogen evolution reaction (HER) will reach 20% of total annual world production of hydrogen [3]. However, current hydrogen energy is mainly produced from natural gas (48%) and other fossil fuels (48%). Only 4% of hydrogen is produced via water electrolysis [4]. As one half-reaction of water electrolysis, the alkaline HER is well-known to be restricted by sluggish kinetics because the HER reaction in alkaline

electrolytes usually needs an additional water dissociation steps by contrast to that in acidic solutions [5]. It is thus difficult to simultaneously achieve high-efficient hydrogen production in universal media, namely in both acidic and alkaline media.

In order to design an electrocatalyst with high HER performance in universal media, its hydrogen intermediates adsorption energy needs to be optimized [6]. According to widely accepted HER volcano plot, a best HER electrocatalyst is located near the top of the volcano plot or with an optimal Gibbs free energy for hydrogen intermediates adsorption (ΔG_{H^*}) [7]. Recently, various strategies have been employed to achieve more optimal ΔG_{H^*} values for different HER electrocatalysts [8,9]. Among them, the nonstoichiometric effect is a tactic to engineering the stoichiometry of chemical compounds to artificially generate vacancies or

* Corresponding authors.

** Corresponding author at: Hunan Province Key Laboratory for Advanced Carbon Materials and Applied Technology, College of Materials Science and Engineering, Hunan University, Changsha 410082, China.

E-mail addresses: zhangqin627@wust.edu.cn (Q. Zhang), xkli8524@sina.com (X. Li), nianjun.yang@uni-siegen.de (N. Yang).

mixed-valence states for prominently transforming the physicochemical properties of the chemical compounds [10]. The characteristic of non-stoichiometric compounds is that their number of anions and cations does not have a definite integer ratio and can be adjusted within a certain range, which exhibits a variety of adjustable electronic structures. Moreover, the introduction of a nonstoichiometric effect into electrocatalysts is systematically verified as one of the most applicable approaches to efficiently enhance the catalytic activity of electrocatalysts [10]. For instance, it can introduce vacancies for inducing an increase of the amount of electrocatalytic active sites of HER, and for optimizing the electronic structures to bring an optimized ΔG_{H^*} . Meanwhile, high-entropy alloys [11] or metallic glass [12,13], metlenes [14], perovskites, [15] and intermetallic [16] that possess multiple reaction sites and favorable ΔG_{H^*} values have been often utilized as the electrocatalysts to boost the sluggish HER kinetics.

Different from most of the reported approaches, we are interested in the design and synthesis of cost-effective HER electrocatalysts, which can exhibit high performance in both acidic and alkaline media. Among the category of metal sulfides, titanium sulfide is the lightest, cheapest, and relatively structural stabilized, but its further improvements on electrocatalyst toward HER are bedeviled by a lack of active sites and obscure intrinsic catalytic traits [17]. Attracted by the various non-stoichiometric ratios and unique electrochemical traits offered by titanium sulfides, nickel sulfide (NiS) with high conductivity, potential electrocatalytic traits, and cost effective [18,19] was utilized to integrate with titanium sulfide (TiS_{2-x}) to form a nonstoichiometric $\text{TiS}_{2-x}/\text{NiS}$ hetero-catalyst. Given the fact that there are 8 electrons presented in the 3d orbital of a Ni atom ($3d^8 4s^2$), whereas there are only 2 electrons presented in the 3d orbital of a Ti atom ($3d^2 4s^2$). This leads to variation in shielding or screening effect. Since a shielding effect influences the amount of nuclear attraction force toward the outermost electron(s) in an atom, more electrons are presented before the outermost electron(s) and the attractive force of the nucleus will be lesser toward the outermost electron(s). In this regard, a Ni atom requires a lesser amount of ionization energy to remove the outermost electrons than a Ti atom. Namely, a Ni atom with a lower ionization enthalpy can more easily lose electrons than a Ti atom. Acting as a reducing agent, a Ni atom is easier to be combined with the S species than a Ti atom. Consequently, a $\text{TiS}_{2-x}/\text{NiS}$ heterointerface is formed, which can simultaneously integrate a nonstoichiometric effect with an interface effect. This heterointerface thus generates abundant sulfur vacancies or increases the reaction sites for the HER and optimizes the d-electronic structure of this catalyst, eventually achieving its high-efficient HER in both alkaline and acid media. In this contribution, we report about the design, synthesis, and characterization of this low-cost and multi-sites-owned $\text{TiS}_{2-x}/\text{NiS}$ HER catalyst as well as its performance toward the HER in both acidic and alkaline media. The HER catalytic mechanisms of this catalyst in both media are also experimentally and theoretically clarified.

2. Experiment

2.1. Chemicals

Pt/C (20 wt%) and Titanium tetrachloride were acquired via Alfa Aesar and Aladdin Co., Ltd, respectively. Changde Liyuan New Material Co., Ltd provide the nickel foam (NF) base, its corresponding parameters are listed in Table S1. Other involved chemicals and reagents purchased from Sinopharm Chemical Reagent Co., Ltd. were of analytical grade. To clear off the superficial oxidized layer, the NF base was conducted through sonication successively in acetone, ethanol, 3 M HCl solution and distilled water. A time of 10 min was applied for each solution/solvent.

2.2. Catalyst synthesis

2.2.1. Preparation of the $\text{TiS}_{2-x}/\text{NF}$ catalyst

A facile solvothermal approach was adopted to synthesize the $\text{TiS}_{2-x}/\text{NF}$ nanosheets. At the beginning, thiourea (0.053 mol) was dispersed in methylbenzene (0.235 mol). This mixture is denoted as solution A. Meanwhile, methylbenzene (0.235 mol) was utilized to dissolve titanium tetrachloride (0.009 mol). This mixture is marked as solution B. Secondly, solution A was mixed with solution B. The resultant mixture was continuously stirred till a homogeneous solution was obtained. The NF base was dipped in this homogeneous solution in a 100 mL Teflon-lined stainless steel autoclave. After that, the autoclave was heated in an electrical oven at 200 °C for 5 h. The products or $\text{TiS}_{2-x}/\text{NF}$ nanosheets were cooled down naturally to room temperature. Ethanol and water were used to repeatedly wash the products. And then as-prepared products were put in vacuum at 80 °C overnight for drying.

2.2.2. Preparation of the $\text{TiS}_{2-x}/\text{NiS}$ catalyst

The as-prepared $\text{TiS}_{2-x}/\text{NF}$ was utilized as the precursor and heated in a tube furnace at 450 °C for 2 h. The used heating rate of sulfidation procedure was 5 °C min⁻¹. The sulfur source applied CS₂ gas. Besides that, nitrogen with a flow rate of 50 mL min⁻¹ served as carrier gas. The final product was the $\text{TiS}_{2-x}/\text{NiS}$ catalyst. The loading mass of this catalyst was altered as required. Under most conditions, a loading amount of 6.10 mg cm⁻² was applied. As a control experiment, sulfidation temperatures of 350 °C and 550 °C were also utilized to prepare $\text{TiS}_{2-x}/\text{NiS}$ catalysts.

2.2.3. Preparation of the TiS_{2-x} catalyst

Conducting the same solvothermal approach as the preparation of the $\text{TiS}_{2-x}/\text{NF}$ catalyst, but not using the NF base, can obtain the TiS_{2-x} catalyst.

2.2.4. Preparation of the NiS catalyst

The single component of the NiS catalyst was synthesized via performing the aforementioned sulfidation procedure (e.g., the preparation of the $\text{TiS}_{2-x}/\text{NiS}$ catalyst) toward the NF substrate.

2.2.5. Preparation of the Pt/C-NF catalyst

The market-available Pt/C catalyst was coated on NF base to fabricate the Pt/C-NF catalyst. At first, a mixture consisting of water (800 μL), ethanol (200 μL), and Nafion solution (40 μL, 10 wt%) was employed to disperse commercial Pt/C (50 mg, 20 wt%) via ultrasonic treatment for few minutes to form a uniform ink. Subsequently, the NF base (1 cm × 1 cm) was covered with ink and dried in air. The loading mass of Pt/C-NF of around 6.10 mg cm⁻² requires 255 μL inks.

2.2.6. Preparation of the TiS_{2-x} -NF and TiS_2 -NF catalysts

Similar as the preparation of the Pt/C-NF catalyst, 50 mg of as-fabricated TiS_{2-x} or 50 mg as-purchased TiS_2 were used to fabricate the TiS_{2-x} -NF and TiS_2 -NF catalysts.

2.3. Characterizations

To affirm the microscopic structures of studied catalysts, field-emission scanning electron microscopy (SEM, TESCAN MIRA3, USA) and high-resolution transmission electron microscopy (HRTEM, Tecnai G2 F20 S-TWIN, USA) were utilized. X-ray diffraction measurements (XRD, MiniFlex-600, Rigaku Corporation., Japan) at a scanning step of 5° min⁻¹ (radiation source of Cu K α , $\lambda = 1.5406 \text{ \AA}$) were conducted to probe into the chemical composition of the catalysts. Raman spectra of as-obtained samples were examined using Raman spectrometer (DXR2, Thermo Fisher Scientific, USA) with a 532-nm excitation laser. X-ray photoelectron spectra of these catalysts were recorded on a X-ray photoelectron spectroscopy (XPS, Thermo Scientific K-Alpha, Thermo Fisher Scientific, USA) assemble with a monochromatic Al K α source.

The ex-situ X-ray absorption spectrometer (XAS, Beamline BL01C1, Taiwan) was performed in the fluorescence mode at room temperature. The S K-edge XAS spectra of the $\text{TiS}_{2-x}/\text{NiS}$ catalyst, the Ti K-edge XAS spectra of the TiS_{2-x} catalyst, and the Ti K-edge XAS spectra of the $\text{TiS}_{2-x}/\text{NiS}$ catalyst were collected. The atomic ratios of these catalysts were recorded by the inductively coupled plasma mass spectrometry (ICP-MS, Agilent 7700 s, Agilent Technologies Inc., USA). A surface area and porosity measurement system (ASAP 2460, Micromeritics Inc., USA) run at 77 K was executed to obtain the nitrogen adsorption/desorption curves of as-prepared catalysts. Gas chromatography (GC-2014 C, Shimadzu Inc., Japan) was applied to quantify hydrogen generated of the $\text{TiS}_{2-x}/\text{NiS}$ catalyst during the HER in both alkaline and acidic media.

2.4. Electrochemical measurements

The catalytic properties of the as-prepared catalysts for HER were examined at room temperature on an electrochemical workstation (1000E, Gamry Instruments, China). An elaborate polytetrafluoroethylene (PTFE) cell was utilized for the electrochemical process. The cell was cleaning and immersing in a piranha solution (~ 98% H_2SO_4 and 30% H_2O_2 , 3:1 v/v) for 24 h and then soaking in distilled water at 90 °C several times to remove the metal impurities. (Notice: use the piranha solution with caution.) The obtained catalysts loaded on NF using extra binders were applied as the working electrode except for the $\text{TiS}_{2-x}/\text{NiS}$ and NiS catalysts. Either 1.0 M KOH (pH = 14) or 0.5 M H_2SO_4 (pH = 0) was served as the electrolytes for the investigation of the HER activities of these catalysts. Electrochemical tests were performed in a three-electrode setup. Thereinto, a graphite rod serves as the counter electrode. In alkaline solutions, an Hg/HgO electrode (potential difference $E^0 = 0.098$ V in 1.0 M KOH electrolyte) was treated as the reference electrode. And the reference electrode apply an Ag/AgCl electrode (potential difference $E^0 = 0.199$ V in 0.5 M H_2SO_4 electrolyte) in acidic media. When scan rate was set at 5 mV s⁻¹, linear sweep voltammograms (LSVs) were measured. The Nyquist plots were evaluated (frequency range: 0.1 Hz to 10⁵ Hz) to examine the charge transfer of catalysts. During the accelerated degradation test (ADT), 1000 replicative cyclic voltammograms (CVs) of the $\text{TiS}_{2-x}/\text{NiS}$ electrocatalyst were recorded in a certain potential window (0 ~ -0.4 V, vs. RHE). The long-term chronoamperometric tests (e.g., for 100 h) were carried out to examine the stability of the $\text{TiS}_{2-x}/\text{NiS}$ electrode in both alkaline and acidic media. To obtain the current densities of 10 and 100 mA cm⁻² in 1.0 M KOH, the applied potentials were set at -0.063 and -0.179 V, respectively. To reach the current densities of 10 and 100 mA cm⁻² in 0.5 M H_2SO_4 , the applied potentials were set at -0.134 and -0.288 V, respectively. The stability of $\text{TiS}_{2-x}/\text{NiS}$ electrocatalyst was also verified under the high current density (e.g., at an industrial scale of 500 mA cm⁻²) for 20 h. The employed potentials were set at -0.258 V (vs. RHE) in 1.0 M KOH or at -0.341 V (vs. RHE) in 0.5 M H_2SO_4 . In this work, all measured potentials (E) were calibrated according to the formula of $E_{\text{RHE}} = E + 0.05916 \text{ pH} + E^0$. In the equation of $\eta = b \log(j) + a$ to calculate the Tafel slopes of these catalysts, η , b , j , and a stand for the overpotential, Tafel slope, current density, and Tafel constant, respectively.

The Electrochemical surface areas (ECSA) of as-obtained catalysts were acquired from cyclic voltammograms (CVs) recorded at different scan rates (e.g., 0.2, 0.25, 0.3, 0.35, 0.4, 0.45, 0.5, 0.55, 0.6, 0.65, 0.7, 0.75, 0.8 V s⁻¹) within a non-faradic reaction zone. A 0.1 V potential window near the open circuit potential was chosen [S1]. The ECSA of a catalyst was elicited with the equation of $\text{ECSA} = C_{\text{dl}}/C_s$, where the double-layer capacitance (C_{dl}) was obtained from the slope of the fitting line. The line was obtained by plotting the half current density (($j_a - j_c$)/2) as a function of scan rate. The specific capacitance of unit area for a smooth planar surface (C_s) of a catalyst was set as 0.04 and 0.035 mF cm⁻² in 1.0 M KOH [S2] and 0.5 M H_2SO_4 [S3], respectively. The roughness factor (R_f) of a catalyst was estimated from the following equation of $R_f = C_{\text{dl}}/C_0$, where C_0 applied the value of 0.06 F cm⁻², the

capacitance of an ideal smooth surface of a metal oxide [S4].

The Faradaic efficiencies (FE) of the $\text{TiS}_{2-x}/\text{NiS}$ catalyst toward the HER were tested at different potentials (e.g., -0.05, -0.10, -0.15, -0.20, and -0.25 V vs. RHE) in 1.0 M KOH. In the electrolyte of 0.5 M H_2SO_4 , the applied potentials included -0.10, -0.15, -0.20, -0.25, and -0.30 V (vs. RHE). The carrier gas was 99.999% ultrapure argon. The values of FE were calculated using the equation of $\text{FE} = n \times m \times V_m / (I_t F)$, where a sum of transferred electrons (n) of 2 was used in this article, m stands for the mole fraction of H_2 , V_m is the flow rate of molar gas in the electrolysis time (t), I denote the current related to the applied voltage.

Calculations on turn over frequency (TOF): According to the methods reported [S5, S6], the per-site TOF was calculated using the equation of:

$$\text{TOF} = \frac{\text{Number of total hydrogen turnovers}/\text{cm}_{\text{geo}}^2}{\text{Number of active sites}/\text{cm}_{\text{geo}}^2}$$

The number of total hydrogen turnovers was:

$$\begin{aligned} & \left(j \frac{\text{mA}}{\text{cm}_{\text{geo}}^2} \right) \left(\frac{1 \text{C s}^{-1}}{100 \text{ mA}} \right) \left(\frac{1 \text{ mol e}^{-1}}{96485 \text{ C}} \right) \left(\frac{1 \text{ mol H}_2}{2 \text{ mol e}^{-1}} \right) \left(\frac{6.022 \times 10^{23} \text{ H}_2 \text{ molecules}}{1 \text{ mol H}_2} \right) \\ & = 3.12 \times 10^{15} \frac{\text{H}_2/\text{s}}{\text{cm}_{\text{geo}}^2} \text{ per } \frac{\text{mA}}{\text{cm}_{\text{geo}}^2} \end{aligned}$$

$$\begin{aligned} \text{Number of active sites (Ti)} &= \frac{\text{Number of atoms/ until cell}^{2/3}}{\text{Volume/unit cell}} \\ &= 1.389 \times 10^{15} \text{ atoms cm}^{-2} \end{aligned}$$

$$\begin{aligned} \text{Number of active sites (Ni)} &= \frac{\text{Number of atoms/ until cell}^{2/3}}{\text{Volume/unit cell}} \\ &= 2.326 \times 10^{15} \text{ atoms cm}^{-2} \end{aligned}$$

Note that, $\text{TiS}_{2-x}/\text{NiS}$ catalyst consisted of 76.75% NiS and 23.25% TiS_{2-x} according to the ICP results (Table S3). Therefore, the active site density of $\text{TiS}_{2-x}/\text{NiS}$ is estimated by using the method suggested by: [S7].

$$(1.389 \times 10^{15} \text{ atoms cm}^{-2} \times 23.25\%) + 2.326 \times 10^{15} \text{ atoms cm}^{-2} \times 76.75\%) \times \text{BET} \times \text{mass} = 2.148 \times 10^{17} \text{ sites cm}^{-2}$$

The current density (j) from the LSV curves is then translated into TOF values according to:

$$\text{TOF} = \frac{\left(3.12 \times 10^{15} \frac{\text{H}_2/\text{s}}{\text{cm}_{\text{geo}}^2} \text{ per } \frac{\text{mA}}{\text{cm}_{\text{geo}}^2} \times |j| \right)}{2.148 \times 10^{17} \text{ sites cm}^{-2}} = 0.0145|j|$$

Thus, the TOF values (-0.15 V vs. RHE) of $\text{TiS}_{2-x}/\text{NiS}$ catalyst in 1 M KOH and 0.5 M H_2SO_4 were 0.81 and 0.26 $\text{H}_2 \text{ S}^{-1}$, respectively.

2.5. Theoretical calculations

The first-principle DFT calculations were conducted by a Vienna Ab initio Simulation Package (VASP) using the projector augmented wave (PAW) method. [S8, S9] The generalized gradient approximation (GGA) of the Perdew-Burke-Ernzerhof (PBE) functional was employed to handle the exchange-functional [S8]. The cut-off energy of the plane-wave basis was fixed in 400 eV to optimize the calculations for atoms and cells. The vacuum spacing in a direction perpendicular to the plane of the catalyst is at least 12 Å. The Brillouin zone integration was executed adopting a 3 × 3 × 1 Monkhorst-Pack k-point sampling for a primitive cell [S10]. The self-consistent calculations were employed with a convergence energy threshold of 10⁻⁵ eV. The equilibrium lattice constants were optimized with the maximum stress on each atom within 0.05 eV Å⁻¹. The Hubbard U (DFT+U) corrections for a 3d-transition metal were set based on the previous reports [S11]. At first, the model of $\text{TiS}_{2-x}/\text{NiS}$ heterostructure has been constructed. Based on the subsequent TEM analysis, it can be seen that $\text{TiS}_{2-x}/\text{NiS}$ heterointerfaces

consist of the (002) facet of TiS_{2-x} and the (100) of NiS. Affected by interfacial effect, these two specific crystal facets nearby the heterointerface would probably display unimaginable catalytic activity than that of other facets. To further verify the catalytic activity of specific facet nearby $\text{TiS}_{2-x}/\text{NiS}$ heterointerfaces, the surfaces of TiS_{2-x} (002), TiS_2 (001), NiS (100) catalysts were built for better comparison. Eventually, the free energies were acquired via the formula of $G = E_{total} + E_{ZPE} TS$, where E_{total} , E_{ZPE} , and TS is the ground-state energy, zero-point energy, and the entropy term, respectively. Namely, chemisorption energies of atomic hydrogen were computed with respect to $\text{H}_2(\text{g})$. The associated free energies of chemisorption were calculated by correcting for both the zero-point vibrational energy and the loss of translation entropy of $\text{H}_2(\text{g})$ on the adsorption, where the smaller vibrational entropy terms were neglected.

3. Results and discussion

3.1. Catalyst characterization

Prior to synthesizing the $\text{TiS}_{2-x}/\text{NiS}$ catalyst, a few properties (e.g., electronic structures, charge transfer, and adsorbed free energy for reaction intermediates) of $\text{TiS}_{2-x}/\text{NiS}$ heterostructure were unveiled, namely the benefits of introducing a nonstoichiometric effect into this catalyst toward the HER were theoretically verified. In the first step, sulfur vacancies were artificially introduced into TiS_2 . Namely, a

nonstoichiometric TiS_{2-x} catalyst was designed. Subsequently, the functional theory (DFT) calculations on the correlative theoretical models, including the NiS, TiS_2 and TiS_{2-x} catalysts were conducted to estimate and further compare their free energies of the adsorption of hydrogen intermediates during the HER process (Fig. S1). The alkaline HER process is generally accepted to begin with a water dissociation process, followed by the H_2 generation process [20]. A glorious HER catalyst is thus expected to possess a ΔG_{H^*} close to 0 eV. Actually, such a HER catalyst holds a balance between the transfer of proton and the secession of adsorbed hydrogen [21]. Meanwhile, a low value of water dissociation energy ($\Delta G_{\text{H}_2\text{O}}$) is essential for a HER catalyst. This is because a small $\Delta G_{\text{H}_2\text{O}}$ value of a HER catalyst indicates facilitated cleavage of the HO–H bond and accelerates the subsequent generation of absorbed hydrogen intermediates (H^*), accordingly leading to a vibrant HER kinetics [6]. In these regards, the $\Delta G_{\text{H}_2\text{O}}$ and ΔG_{H^*} values on the various adsorption sites (e.g., Ti, Ni, S) of the NiS, TiS_2 and TiS_{2-x} catalysts toward the alkaline HER were calculated. From the corresponding diagrams (Fig. 1a), one can see that metallic Ti and Ni sites display higher HER catalytic activities than S sites in those catalysts. Remarkably, the Ti sites in the TiS_{2-x} catalyst feature outstanding activities in terms of both water dissociation and hydrogen intermediates adsorption. Its superior ability over other two catalysts can be ascribed to the introduction of sulfur vacancies in this nonstoichiometric catalyst, which invests an uncoordinated Ti site with an electron-rich structure to efficiently adsorb hydrogen [22]. Based on these theoretical simulation

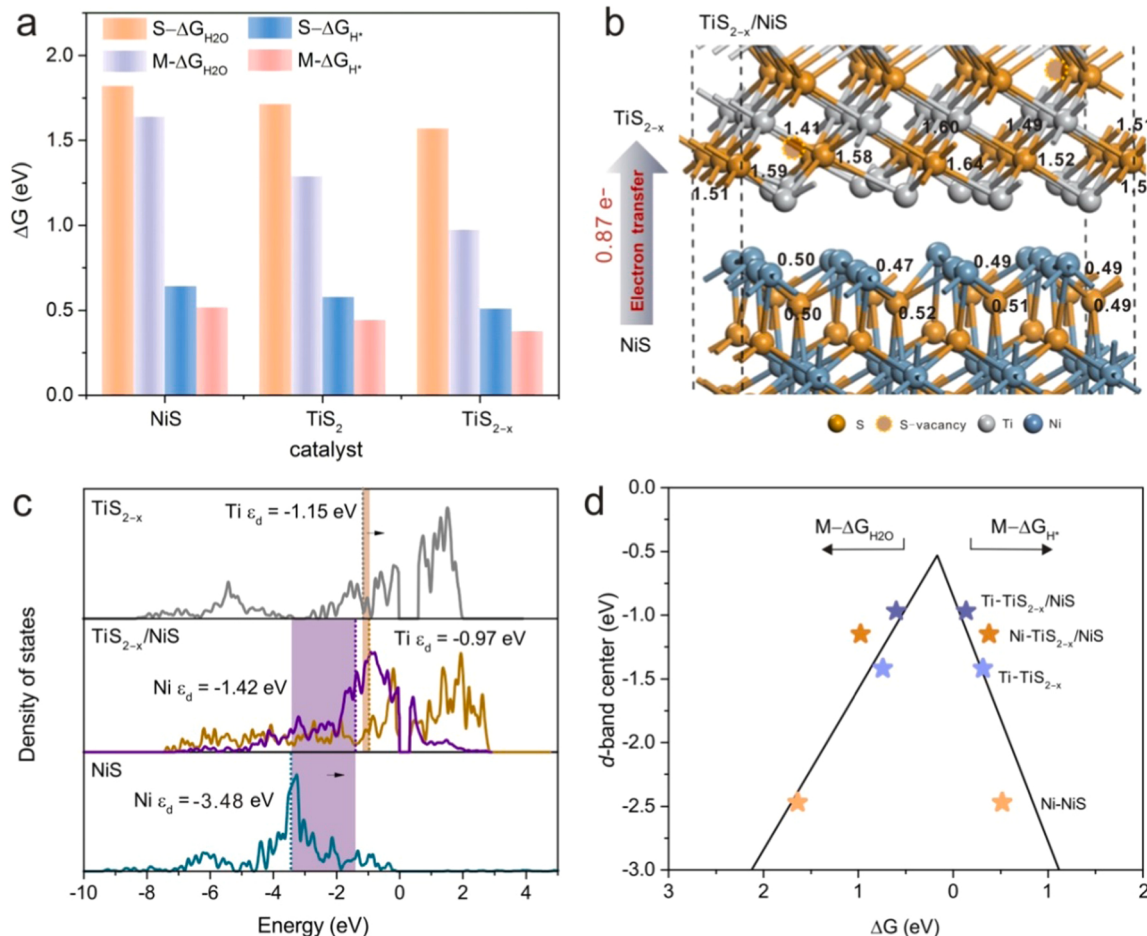


Fig. 1. The DFT calculations of a $\text{TiS}_{2-x}/\text{NiS}$ catalyst: (a) The calculated free energy for alkaline HER on the S site ($S-\Delta G_{\text{H}_2\text{O}}$ and $S-\Delta G_{\text{H}^*}$) and metal (Ti or Ni) sites; $M-\Delta G_{\text{H}_2\text{O}}$ and $M-\Delta G_{\text{H}^*}$) of the NiS, TiS_2 and TiS_{2-x} catalysts; (b) Bader charge analysis of S cations via a $\text{TiS}_{2-x}/\text{NiS}$ heterointerface inside the $\text{TiS}_{2-x}/\text{NiS}$ catalysts; (c) The calculated partial density of states (DOS) curves and d-band centers (ϵ_d) of the NiS, TiS_{2-x} and $\text{TiS}_{2-x}/\text{NiS}$ catalysts; (d) Volcano plot based on the relationship between d-band centers and the calculated free energies of hydrogen adsorption and water dissociation on the metal (Ti or Ni) sites ($M-\Delta G_{\text{H}_2\text{O}}$ and $M-\Delta G_{\text{H}^*}$) of the NiS, TiS_{2-x} and $\text{TiS}_{2-x}/\text{NiS}$ catalysts.

results, a model of $\text{TiS}_{2-x}/\text{NiS}$ hetero-catalyst featuring multi-sites was constructed (Fig. S2) with an attempt to promote the HER performances. The differential charge density (Fig. S3) was then calculated together with its Bader charge analysis (Fig. 1b). An amount of 0.87 e^- charge transport is demonstrated from the NiS phase to the TiS_{2-x} phase near the $\text{TiS}_{2-x}/\text{NiS}$ heterointerface. This electron transfer makes the TiS_{2-x} phase have more electron-rich states. In this regard, the $\text{TiS}_{2-x}/\text{NiS}$ catalyst is in favor of the optimized hydrogen adsorption energy on Ti sites. Moreover, the formation of a $\text{TiS}_{2-x}/\text{NiS}$ heterointerface significantly raises the density of state (DOS) around Fermi level (Fig. S4). Consequently, a strengthened conductivity of a $\text{TiS}_{2-x}/\text{NiS}$ catalyst and its facilitated electrochemical kinetics via the accelerated electron transfer and improved carrier density are expected to be achieved.

The calculations of the *d*-band centers of the TiS_{2-x} , NiS, and $\text{TiS}_{2-x}/\text{NiS}$ catalysts (Fig. 1c) were also executed to give an in-depth probe on the consequences of interfacial charge transfer for electronic structures of these catalysts. For the $\text{TiS}_{2-x}/\text{NiS}$ catalyst, its *d*-band center of Ti (-0.97 eV) upshifts relative to the Fermi level, when compared to that (-1.15 eV) of the TiS_{2-x} catalyst. Meanwhile, the *d*-band center of Ni active sites in the $\text{TiS}_{2-x}/\text{NiS}$ (-1.42 eV) catalyst moves up in contrast to that (-3.48 eV) of the NiS catalyst, which endows the Ti and Ni sites in the $\text{TiS}_{2-x}/\text{NiS}$ catalyst with an increased adsorbing strength of

hydrogen intermediates [23,24].

Based on the *d* band theory, when the adsorbed hydrogen intermediates hybridizes with the *d* band of $\text{TiS}_{2-x}/\text{NiS}$, the adsorbate state would split into localized bonding and antibonding states [25]. The higher position of the antibonding could bring the stronger $\text{TiS}_{2-x}/\text{NiS}-\text{H}$ interaction. Thus, the antibonding states upshift to higher energy position, leading to lower occupancy and thereby cause stronger H^* adsorption. According to the above analysis, one Volcano plot was then drawn to explore the relationship between *d*-band centers and the adsorption for H^* (the calculated ΔG_{H^*}) and water dissociation (the calculated $\Delta G_{\text{H}_2\text{O}}$) of the NiS, TiS_{2-x} and $\text{TiS}_{2-x}/\text{NiS}$ catalysts (Fig. 1d). Clearly, those catalysts with *d*-band centers (Ti or Ni) close to Fermi level possess the optimal ΔG_{H^*} values and low $\Delta G_{\text{H}_2\text{O}}$. Therefore, it can be inferred that the $\text{TiS}_{2-x}/\text{NiS}$ catalyst located near the volcano top exhibits optimized ΔG_{H^*} and $\Delta G_{\text{H}_2\text{O}}$ values and thus a potential HER electrocatalyst.

According to the design of the $\text{TiS}_{2-x}/\text{NiS}$ catalysts theoretically predicted from the above DFT calculation results, a $\text{TiS}_{2-x}/\text{NiS}$ catalyst was synthesized by means of a simple two-step procedure (Fig. 2a). In the first step, a three-dimensional (3D) porous Ni foam (labelled as NF) is applied as the substrate to support the growth of nonstoichiometric TiS_{2-x} nanosheets, where a solvothermal treatment is applied in the

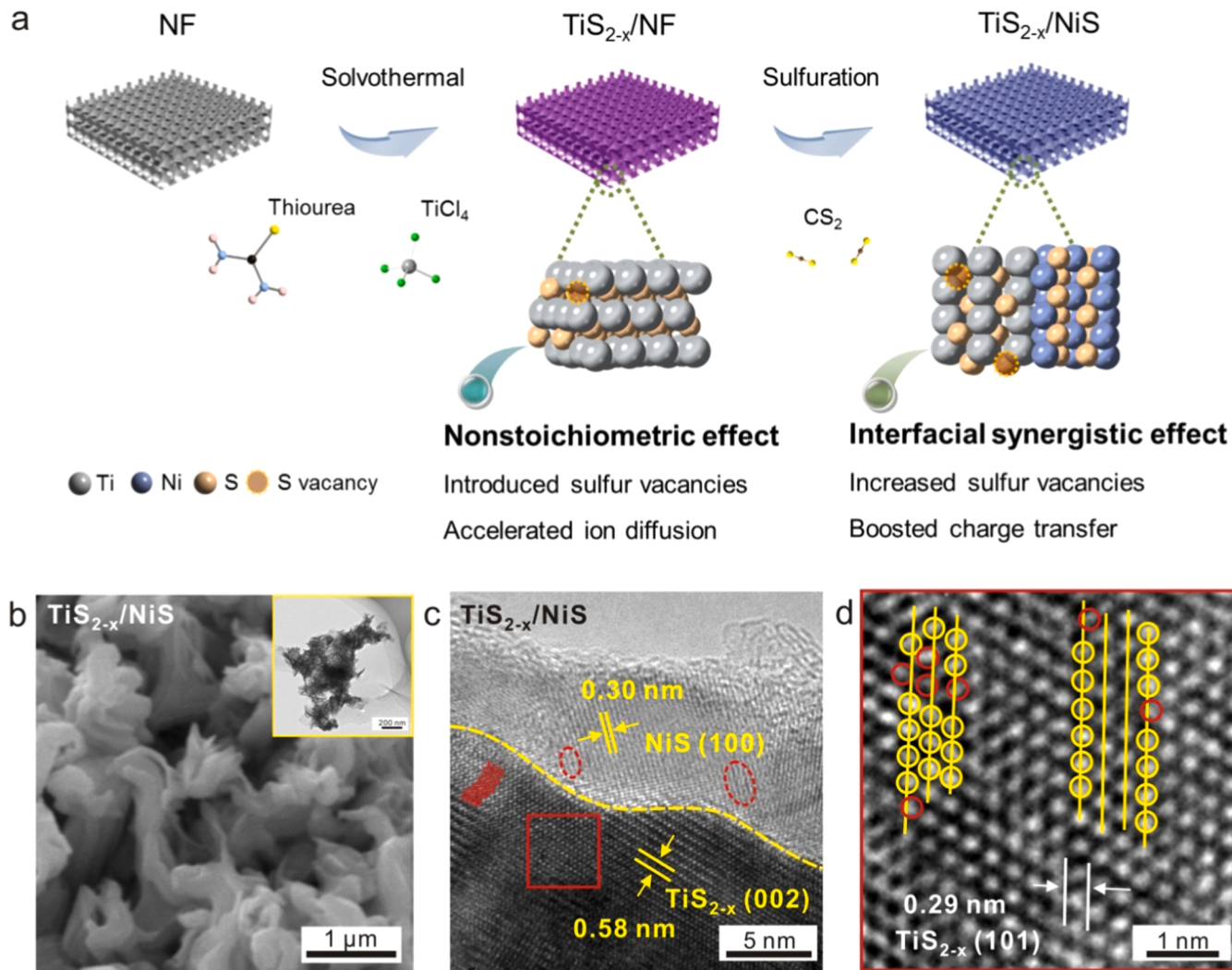


Fig. 2. Characterization of the $\text{TiS}_{2-x}/\text{NiS}$ catalyst: (a) Schematic illustration of the synthesis steps of the $\text{TiS}_{2-x}/\text{NiS}$ electrocatalyst; (b) SEM images of the $\text{TiS}_{2-x}/\text{NiS}$ catalyst. Inset of (b): TEM image of the $\text{TiS}_{2-x}/\text{NiS}$ catalyst; (c) High-resolution TEM (HRTEM) image of the $\text{TiS}_{2-x}/\text{NiS}$ catalyst. A heterointerface is designated by a yellow dotted line and the lattice distortion nearby the heterointerface is marked with red dotted circles and wavy lines; (d) The magnified HRTEM images recorded from the marked red regions in (c). Yellow circles indicate non-deformed crystal facets and the red circles display slightly deformed crystal facets.

presence of thiourea and titanium tetrachloride. Under the action of a nonstoichiometric effect, as-grown TiS_{2-x} nanosheets are assembled with sulfur vacancies, which can accelerate the ion diffusion. In the sequent sulfuration treatment, the NF substrate is thoroughly transformed into the NiS phase with the help of a CS_2 precursor. Taking the migration of nickel into consideration, the sulfuration temperature was a key to achieving the successful preparation of tight $\text{TiS}_{2-x}/\text{NiS}$ heterostructures. Thus, three sulfuration temperatures varying from 350 °C, 450–550 °C were carefully explored their effects on the morphology of heterostructures. As shown in Fig. S5, $\text{TiS}_{2-x}/\text{NiS}$ catalyst synthesized under 450 °C exhibits morphology consisting of uniform nanosheets, differing from the mixed morphology under 350 °C or the large block shape under 550 °C. The sulfuration temperature of 350 °C is too low to provide power to support the migration of Ni, resulting in the independent TiS_{2-x} nanosheets and NiS nanoparticles. And the sulfuration temperature of 550 °C is too high to cause the overgrowth and agglomeration of products. Therefore, 450 °C was adopted as the optimal sulfuration temperature to guarantee the successful acquirement of $\text{TiS}_{2-x}/\text{NiS}$ catalyst. During the sulfuration at this proper temperature of 450 °C, the as-synthesized NiS phase migrates or diffuses, and grows upward along the TiS_{2-x} nanosheets from the base, gradually intertwining and wrapping the TiS_{2-x} nanosheets. In view of the fact that the ionization energy of Ni atom is smaller than that of Ti, a Ni atom is thus more easily combined with a S atom than a Ti atom. In this context, the formation of a $\text{TiS}_{2-x}/\text{NiS}$ heterointerface is induced during the course of this sulfuration treatment. Note that the generation of a heterointerface on a hetero-catalyst is usually accompanied with an interfacial synergistic effect, which likely magnify in turn the existing nonstoichiometric effect. Consequently, the density of vacancies near the heterointerface increases, leading to promoted carrier density and accelerated charge transport [8]. In other words, it can be hypothesized that the incorporation of a NiS phase into the TiS_{2-x} catalyst, namely the construction of the $\text{TiS}_{2-x}/\text{NiS}$ heterostructure can probably boost the nonstoichiometric effect and eventually help to achieve satisfactory HER catalytic activity.

To support such an assumption, the $\text{TiS}_{2-x}/\text{NiS}$ catalyst was then characterized using different techniques. As control experiments, the NF and $\text{TiS}_{2-x}/\text{NF}$ catalysts were also characterized with these techniques. From their scanning electron microscopy (SEM) images (Fig. S6), one can clearly see the morphological evolution of these catalysts in the course of the preparation of the $\text{TiS}_{2-x}/\text{NF}$ catalyst. For example, the surface of the used NF (Table S1,) is clean and smooth (Fig. S6a). After the application of the solvothermal process, TiS_{2-x} nanosheets are thoroughly coated on the surfaces of the NF. Their size is about 200 ~ 250 nm (Fig. S6b). The EDS examination of $\text{TiS}_{2-x}/\text{NF}$ catalyst (Fig. S7) reveals that there probably exist slight by-products (NiS and NiO) except for the main product of TiS_{2-x} . It is relatively hard to verify NiS form in the bottom of the TiS_{2-x} /NF catalyst or not because the surface of $\text{TiS}_{2-x}/\text{NF}$ is covered by luxuriant TiS_{2-x} nanosheets. However, when the NF base experienced the same solvothermal process without adding Ti source, there generated Ni_3S_2 , whose XRD pattern was shown in Fig. S8. The by-products of Ni_3S_2 have been proved to exist which is caused by the participation of the nickel foam base in the solvothermal reaction. And they could be transformed into NiS to construct $\text{TiS}_{2-x}/\text{NiS}$ in the subsequent sulfidation. Besides that, the TiS_{2-x} catalyst used for structural characterization was synthesized under the identical solvothermal reaction but without the participation of Ni foam. Also, the as-synthesized TiS_{2-x} was made into ink to cover on the Ni foam (with the help of binder) to prepare $\text{TiS}_{2-x}/\text{NF}$ catalyst as a contrast in the following electrochemical measurement. Hence, the by-products brought by the solvothermal process do no effect on the whole experiment. When the sulfidation treatment is employed, continuous nanosheets are observed in the SEM image of the $\text{TiS}_{2-x}/\text{NiS}$ catalyst (Fig. 2b). The morphology difference of this catalyst before and after the sulfidation process can be a result of the successful synthesis of a $\text{TiS}_{2-x}/\text{NiS}$ hetero-catalyst. Similarly, the NiS catalyst synthesized on the NF

under the identical conditions displays an analogous structure of nanosheets (Fig. S6c-d).

The subtle structure of the $\text{TiS}_{2-x}/\text{NiS}$ catalyst was then checked with transmission electron microscopy (TEM) at diverse magnifications. Continuous nanosheets are observed, comprising subunits of smaller nanosheets that are interlinked with each other (inset of Fig. 2b). In the high-resolution TEM (HRTEM) of the $\text{TiS}_{2-x}/\text{NiS}$ catalyst (Fig. 2c), the lattice fringe of about 0.58 nm is related to the (002) plane of the TiS_{2-x} phase, while the lattice distance of 0.30 nm appertains to the (100) plane of the NiS phase. To guide the eyes, the heterointerface between the TiS_{2-x} phase and the NiS phase is designated by a yellow imaginary line. The lattice distortions nearby the heterointerface can be clearly observed, marked with red dotted circles and wavy lines. From the magnified HRTEM image of the zones that are marked with red solid rectangle near the heterointerface (Fig. 2d), no deformed (101) crystal facets on the TiS_{2-x} phase (yellow circles) are seen, while some slightly deformed crystal (101) facets on the of TiS_{2-x} phase (red circles) are found. This phenomenon is probably originated from the formation of a heterointerface between two phases as well as the introduction of S-vacancies into this catalyst [26]. To further verify the existence of S-vacancies, a TEM image of $\text{TiS}_{2-x}/\text{NiS}$ catalyst with an atomic resolution was supplied in Fig. S9. It is obvious that S-vacancies exist at the zone of TiS_{2-x} , designated by yellow box for guiding the eyes. Additionally, the elemental mapping (Fig. S10) of the $\text{TiS}_{2-x}/\text{NiS}$ catalyst was conducted, where the uniform presence of Ti, Ni and S atoms on this catalyst is manifested, again affirming the growth of a NiS phase along the direction of the TiS_{2-x} phase. The atomic ratio between Ni and S was assumed as 1. Based on the atomic percentage of $\text{TiS}_{2-x}/\text{NiS}$ catalyst from X-ray energy dispersive spectrum (EDS) spectrum (Fig. S11), the rest of the S atoms are less than twice as much as Ti atoms after subtracting the S atoms related to Ni, thus it can roughly reveal the deficiency of sulfur atoms in $\text{TiS}_{2-x}/\text{NiS}$.

To ascertain the respective phase composition, X-ray diffraction (XRD) analysis was executed on the NF, NiS, TiS_{2-x} (Fig. S12) and $\text{TiS}_{2-x}/\text{NiS}$ catalysts. The diffraction peaks of the used NF substrate are located at 20 of 44.5°, 51.9° and 76.4°, derived from the (111), (200), and (220) planes of a cubic Ni structure (JCPDS no. 04–0850), respectively. The diffraction peaks of the TiS_{2-x} catalyst appear at 20 of 15.4°, 31.1°, 34.1°, 38.4°, 50.3°, 53.5°, 56.1° and 65.1°, corresponding to the (002), (101), (102), (103), (105), (110), (112), and (202) planes of a hexagonal TiS_{2-x} structure (JCPDS no. 41–0930), respectively. These peaks showed at 20 of 30.2°, 34.7°, 46.0°, 53.6°, 60.9°, 62.7°, 65.7°, 70.8°, 73.3° and 79.08° in the XRD patterns of the NiS catalyst belong to the (100), (101), (102), (110), (103), (200), (201), (004), (202), and (104) planes of a hexagonal phase NiS (JCPDS no. 02–1280), respectively. In the XRD patterns of the $\text{TiS}_{2-x}/\text{NiS}$ catalyst (Fig. S13), both TiS_{2-x} and NiS related XRD peaks are seen, verifying again the successful formation of a $\text{TiS}_{2-x}/\text{NiS}$ heterointerface upon the applied sulfidation procedure.

Raman spectra of the NiS, TiS_{2-x} and $\text{TiS}_{2-x}/\text{NiS}$ catalysts were also recorded in order to confirm the existence of both TiS_{2-x} and NiS phases (Fig. 3a). Both the NiS and $\text{TiS}_{2-x}/\text{NiS}$ catalysts display a noticeable resonance at 860 cm^{-1} , corresponding to the vibration of a NiS phase. In both Raman spectra of the $\text{TiS}_{2-x}/\text{NiS}$ and TiS_{2-x} catalysts, three recognizable resonances appear at 210, 333, and 380 cm^{-1} . The first two modes are indexed to the E_g and A_{1g} modes of the TiS_{2-x} phase, respectively [27]. The third vibrational mode is probably attributed to S-vacancies in these catalysts [28]. Note that not all vibrational modes of both NiS and TiS_{2-x} phases can be observed for these small-sized NiS and TiS_{2-x} nanosheets. This is because these vibrational modes are dependent on the vibration of the crystal lattices [29]. To estimate the density of S-vacancies in as-obtained catalysts, electron paramagnetic resonance (EPR) was executed (Fig. 3b), the EPR was also carried out on the as-purchased TiS_2 as a comparison (Fig. S14). Among these catalysts, only the TiS_{2-x} and $\text{TiS}_{2-x}/\text{NiS}$ catalysts possess a conspicuous EPR signal, of which g-factor value is located at 2.003. This result symbolizes

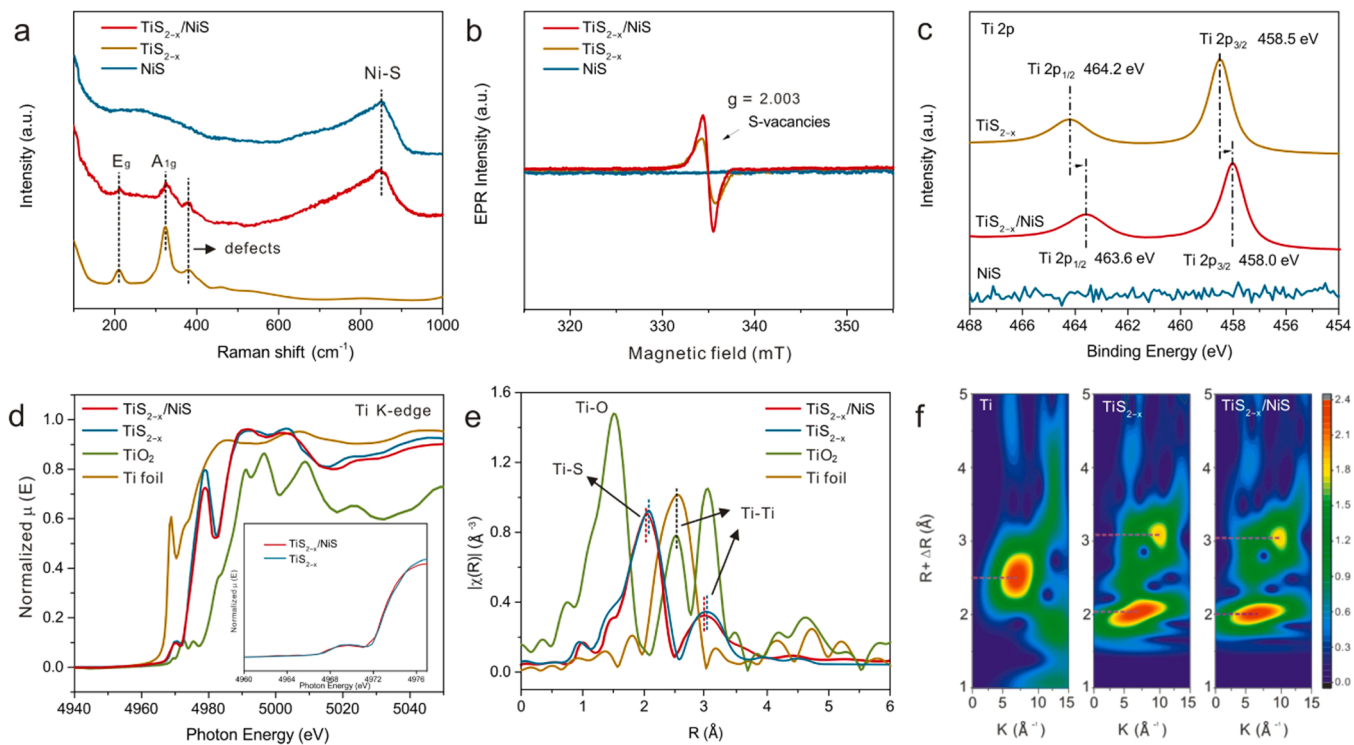


Fig. 3. Characterization of the $\text{TiS}_{2-x}/\text{NiS}$ catalyst: (a) Raman spectra and (b) Room-temperature EPR spectra of the TiS_{2-x} , NiS and $\text{TiS}_{2-x}/\text{NiS}$ catalysts; (c) High-resolution XPS spectra of the Ti 2p spectra of the TiS_{2-x} , NiS and $\text{TiS}_{2-x}/\text{NiS}$ catalysts; (d) The normalized XANES spectra at the Ti K-edge of the TiS_{2-x} and $\text{TiS}_{2-x}/\text{NiS}$ catalysts as well as a Ti foil and a TiO_2 film; (e) FT-EXAFS curves at the Ti K-edge of the TiS_{2-x} and $\text{TiS}_{2-x}/\text{NiS}$ catalysts; (f) Wavelet transforms for the k^3 -weighted Ti K-edge EXAFS signals of a Ti foil as well as the TiS_{2-x} and $\text{TiS}_{2-x}/\text{NiS}$ catalysts.

the emergence of S-vacancies in the TiS_{2-x} and $\text{TiS}_{2-x}/\text{NiS}$ catalysts [30]. The key role of sulfuration temperatures play in the morphology of $\text{TiS}_{2-x}/\text{NiS}$ catalyst has been investigated hereinbefore. Thereinto, the variation and optimization of S-vacancy raises curiosity. Hence, the EPR spectra of $\text{TiS}_{2-x}/\text{NiS}$ catalysts synthesized at 350°C , 450°C , and 550°C have been provided in Fig. S15. As the sulfuration temperature goes up, the S-vacancies density increases at first and then decreases, the line width (distance between the highest and lowest point) continuously shortens. Catalysts approach the ideal conditions along with temperature going up induces the continuously narrowing line width. The incipient rise of S-vacancies derives from the nonstoichiometric effect which is intensified by increased heterointerfaces. Subsequently, the keep going elevated sulfuration temperature ensures more sufficient sulfuration of electrocatalyst which induces the decrease of S-vacancies. Therefore, sulfuration temperature is vital for the optimization of S-vacancy on $\text{TiS}_{2-x}/\text{NiS}$ catalyst, and a moderate sulfuration temperature of 450°C could guarantee the $\text{TiS}_{2-x}/\text{NiS}$ catalyst with abundant S-vacancies. Notably, the intensity of EPR signal is obviously higher for the $\text{TiS}_{2-x}/\text{NiS}$ catalyst when compared with the TiS_{2-x} catalyst (Fig. 3b). In other words, the formation of a $\text{TiS}_{2-x}/\text{NiS}$ heterointerface leads to an increased density of sulfur vacancies. To further verify this statement, the analysis of three catalysts by means of inductively coupled plasma mass spectrometry (ICP-MS) (Table S2) was performed. In the ICP-MS spectrum of the TiS_{2-x} catalyst, the chemical formula of the TiS_{2-x} catalyst is $\text{TiS}_{1.68}$. After NiS incorporating into TiS_{2-x} to form $\text{TiS}_{2-x}/\text{NiS}$ heterointerfaces, the chemical formula of $\text{TiS}_{2-x}/\text{NiS}$ catalyst is $\text{TiS}_{1.47}/\text{NiS}$. In this context, the constitution of this heterointerface indeed increases the density of formed S-vacancies. Since these S-vacancies help to prompt electron movement via changing the electron density of a catalyst and to effectively decrease the energy barrier of a catalytic reaction [26], the $\text{TiS}_{2-x}/\text{NiS}$ catalyst with rich S-vacancies in our case is thus beneficial to bring in an under-coordinated Ti region with electron-rich states. Consequently, the electronic structure of Ti

sites on the $\text{TiS}_{2-x}/\text{NiS}$ catalyst is optimized [22].

Surface chemical formation and interfacial interaction of the $\text{TiS}_{2-x}/\text{NiS}$ catalyst were then probed with aid of X-ray photoelectron spectroscopy (XPS) analysis. In the Ti 2p XPS spectrum of TiS_2 catalyst (Fig. S16), the peaks at 458.7 and 464.4 eV are ascribed to Ti^{2+} and Ti^{3+} , respectively. They confirm the existence of Ti^{4+} in the TiS_2 catalyst [31]. Surprisingly, the related Ti 2p peaks of TiS_{2-x} catalyst negatively shift to 458.5 and 464.2 eV when sulfur vacancies were introduced (Fig. 3c), which prove that the existence of S-vacancies can cause the nearby Ti atoms keep electron-rich state. After the incorporation of a NiS ingredient, two corresponded Ti 2p peaks of the $\text{TiS}_{2-x}/\text{NiS}$ catalyst appear with lower binding energies: Ti^{2+} at 457.8 eV and Ti^{3+} at 463.7 eV. Although they are still indexed to the form of Ti^{4+} [17], such negative shifts of these binding energies prove that the Ti atoms are even more electron-rich, leading to an decrease of oxidation numbers. Obviously, the spontaneously formed heterointerface at the grain boundary between TiS_{2-x} and NiS phases of the $\text{TiS}_{2-x}/\text{NiS}$ catalyst is responsible for these further negative shifts on binding energies of Ti. In this regard, the deviation of electron cloud occurs from the NiS phase to the TiS_{2-x} phase under the electrostatic attraction, resulting in more electrons around Ti sites/centers [9]. Consequently, the introduction of sulfur vacancies and the incorporation of the NiS phase into the TiS_{2-x} catalyst all leads to the enriched electrons on the Ti sites in the $\text{TiS}_{2-x}/\text{NiS}$ catalyst.

The Ni 3d XPS peaks of the $\text{TiS}_{2-x}/\text{NiS}$ catalyst (Fig. S17) emerge at 853.2 and 870.4 eV, associated with Ni^{2+} and Ni^{3+} species, respectively. They shift toward higher binding energies when compared with those of the NiS catalyst (852.9 and 870.1 eV, respectively). In other words, the existence of strong electronic interaction is verified between the TiS_{2-x} phase and the NiS phase, arousing the formation of a $\text{TiS}_{2-x}/\text{NiS}$ heterointerface [32,33].

In the S 2p XPS spectrum (Fig. S18), the S 2p peaks of the NiS catalyst located at 161.4 and 162.5 eV are assigned to the S^{2-} species [32]. As for

the S 2p XPS spectrum of the TiS_{2-x} catalyst, the S 2p peaks presented at 160.9, 162.1 and 163.3 eV are also from the S^{2-} species, while the peaks with the binding energies of 163.9 and 164.6 eV are connected with the S_x^{2-} species [34]. In the S 2p XPS spectrum of the $\text{TiS}_{2-x}/\text{NiS}$ catalyst, the S element exists in two kinds of valence states: the peaks at 161.2, 162.4 and 163.4 eV are corresponds to the S^{2-} species, while those at 163.9 and 164.6 eV are related to the S_x^{2-} species. It is worth mentioning that both rich electrons around Ti sites/centers and the powerful coupling interaction between the TiS_{2-x} phase and the NiS phase in the $\text{TiS}_{2-x}/\text{NiS}$ catalyst are benefit for accelerating HER kinetics [5,35]. Notably, the exact formula of the TiS_{2-x} and $\text{TiS}_{2-x}/\text{NiS}$ catalysts were supplied in Table S3 via the quantitative XPS data, which match well with the results of ICP measurements.

The electronic and coordination structures of the $\text{TiS}_{2-x}/\text{NiS}$ catalyst were further investigated using X-ray absorption spectroscopy. The S K-edge X-ray absorption near-edge structure (XANES) was employed to explain the orbital hybridization degree of the $\text{TiS}_{2-x}/\text{NiS}$ catalyst (Fig. S19). The peak A at 2472 eV arises from the strong $d-p$ orbital hybridization between an unoccupied antibonding sulfur 3p state and an empty transition-metal (Ti or Ni) 3d state. Since both states are related with e_g bandlike states, characteristics of transition-metal sulfides can be studied [36]. This strong $d-p$ orbital hybridization is expected to lead to the delocalization of electronic distribution over metal-ligand units [37], eventually to expose potential catalytic sites of the $\text{TiS}_{2-x}/\text{NiS}$ catalyst. The broad peak B at 2480 eV stems from the hybridization between a sulfur 3p state and a transition-metal 4s or 4p state [38]. The various post-edge features of the following broad peak C at 2485 eV and peak D at 2490 eV are induced by multiple scattering resonances [39].

The XANES spectra of Ti K-edge for the $\text{TiS}_{2-x}/\text{NiS}$ and TiS_{2-x} catalysts as well as a TiO_2 film and a Ti foil were also recorded (Fig. 3d). The pre-edge feature at 4970 eV for the TiO_2 , TiS_{2-x} and $\text{TiS}_{2-x}/\text{NiS}$ catalysts is attributed to the dipole, allowed transition from 1s to 3d orbitals. This hints again the presence of the Ti^{4+} species in these catalysts [40]. In contrast to that of the TiS_{2-x} catalyst, the pre-edge peak intensity of Ti in the $\text{TiS}_{2-x}/\text{NiS}$ catalyst decreases, manifesting that the local environment of Ti in the $\text{TiS}_{2-x}/\text{NiS}$ catalyst owns a higher symmetry [41]. The K-edge positions of Ti in the $\text{TiS}_{2-x}/\text{NiS}$ catalyst and the TiS_{2-x} catalyst were then computed through integrating the nearly linearship of the rising edge of the XANES spectra. The calculated Ti K-edge position in the $\text{TiS}_{2-x}/\text{NiS}$ catalyst is 4973.13 eV, while that in the TiS_{2-x} catalyst is 4973.29 eV. Such difference demonstrates the reduction of oxidation numbers for Ti in the $\text{TiS}_{2-x}/\text{NiS}$ catalyst after the generation of a heterointerface. This phenomenon is the consequence of the electron transfer occurred from the NiS phase to the TiS_{2-x} phase in the $\text{TiS}_{2-x}/\text{NiS}$ catalyst. The main absorption peak of the TiS_{2-x} and $\text{TiS}_{2-x}/\text{NiS}$ catalysts at 4989 eV is then generated from the dipole allowed transition of 1s to 4p orbitals, similar in their intensities and positions [38].

Meanwhile, the Fourier transform (FT) of the Ti extended X-ray absorption fine structure (EXAFS) analysis for the $\text{TiS}_{2-x}/\text{NiS}$ and TiS_{2-x} catalysts as well as a TiO_2 film and a Ti foil was conducted (Fig. 3e) to confirm the change of coordination structures inside the $\text{TiS}_{2-x}/\text{NiS}$ catalyst. Regarding the R space of the TiS_{2-x} catalyst, two identifiable peaks arise at 2.10 and 3.07 Å, ascribed to the lengths of Ti–S and Ti–Ti bonds, respectively [42]. In contrast, the lengths of Ti–S and Ti–Ti bonds in the $\text{TiS}_{2-x}/\text{NiS}$ catalyst shorten to 2.01 and 2.98 Å, respectively. Such shortened bonds are potentially conducive for electron transport between the TiS_{2-x} phase and the NiS phase inside the catalyst. It is worth mentioning that the special electron configuration ($t_{2g}^0 e_g^0$) of Ti^{4+} offers enriched and empty d orbitals, which can boost binding abilities with hydrogen and hydroxyl ions. In this regard, in the $\text{TiS}_{2-x}/\text{NiS}$ catalyst is favor for water dissociation.

Furthermore, wavelet transform (WT) was executed to further probe the Ti K edge EXAFS oscillations. In line with the FTs, a maximum intensity of the WT contour plots is at 7.1 \AA^{-1} for a Ti foil (Fig. 3f) since it is dominated by the Ti–Ti contribution. The maximum intensities at

lower K-space occur in 6.9 and 6.7 \AA^{-1} for the TiS_{2-x} and $\text{TiS}_{2-x}/\text{NiS}$ catalysts, respectively. This is caused by the Ti–S contributions from the metal sulfide structures. This negative shift of the maximum intensity in the $\text{TiS}_{2-x}/\text{NiS}$ catalyst in contrast to that of the TiS_{2-x} catalyst is probably ascribed to the charge transfer from the NiS phase to the TiS_{2-x} phase. Hence, these aforementioned consequences collectively clarify the enhanced conductivity of the $\text{TiS}_{2-x}/\text{NiS}$ catalyst. A strong electron coupling interaction derived from the formation of an atomically dense heterointerface is expected in the $\text{TiS}_{2-x}/\text{NiS}$ catalyst.

3.2. HER performance on the $\text{TiS}_{2-x}/\text{NiS}$ catalyst

To verify the idea that the $\text{TiS}_{2-x}/\text{NiS}$ catalyst owning the non-stoichiometric effect and multi-sites can boost the HER kinetics, the linear sweep voltammograms (LSVs) of the TiS_{2-x} , TiS_2 , NiS and $\text{TiS}_{2-x}/\text{NiS}$ catalysts were recorded using a typical three-electrode configuration in both 1.0 M KOH solution and 0.5 M H_2SO_4 . For the sake of eliminating the influence of high activity derived from a high specific area of the catalysts, the Ni foam (NF) was utilized as a supporting carrier to substitute a commonly used glassy carbon electrode. The synthesized NiS and $\text{TiS}_{2-x}/\text{NiS}$ catalysts reserving the self-supported structure of NF could be directly used as working electrodes without binders. To assess and compare electrocatalytic HER activities of other powder catalysts (e.g., Pt/C, TiS_{2-x} , and TiS_2), NF loaded the Pt/C, TiS_{2-x} , and TiS_2 with an identical loading mass as $\text{TiS}_{2-x}/\text{NiS}$ catalyst (labelled as Pt/C-NF, TiS_{2-x} -NF, and TiS_2 -NF, respectively). The details of the used ink load method were supplied in the experiment section. Moreover, the HER activity of the NF toward the HER is negligible (Fig. S20). Judged from the polarization curves of these catalysts or their LSVs in 1.0 M KOH solution (Fig. 4a), remarkable catalytic activity of the $\text{TiS}_{2-x}/\text{NiS}$ catalyst towards the HER is clearly seen. The overpotential of the $\text{TiS}_{2-x}/\text{NiS}$ catalyst just reaches 63 mV when a current density of -10 mA cm^{-2} is obtained, which is inferior to that (39 mV) of the market-available Pt/C-NF catalyst. The measured Tafel slope of the $\text{TiS}_{2-x}/\text{NiS}$ catalyst is 43.6 mV dec^{-1} (Fig. 4b), fairly close to that of the Pt/C-NF catalyst (40.2 mV dec^{-1}), but far smaller than that of the NiS ($152.5 \text{ mV dec}^{-1}$), TiS_{2-x} -NF (88.9 mV dec^{-1}) and TiS_2 -NF ($110.6 \text{ mV dec}^{-1}$) catalysts. Meanwhile, the $\text{TiS}_{2-x}/\text{NiS}$ catalyst displays outstanding HER performance in 0.5 M H_2SO_4 electrolyte (Fig. 4c) with an overpotential of 134 mV to attain a current density of 10 mA cm^{-2} . Related Tafel slope is 80.9 mV dec^{-1} (Fig. 4d), much lower than that of the NiS ($191.8 \text{ mV dec}^{-1}$), TiS_{2-x} -NF ($232.1 \text{ mV dec}^{-1}$) and TiS_2 -NF ($245.2 \text{ mV dec}^{-1}$) catalysts. The overpotentials for the HER on the as-prepared three catalysts to harvest -10 mA cm^{-2} and -100 mA cm^{-2} in both 1.0 M KOH and 0.5 M H_2SO_4 solutions are then compared (Fig. 4e). To achieve a current density of -10 mA cm^{-2} during the HER in 1.0 M KOH solution, the $\text{TiS}_{2-x}/\text{NiS}$ catalyst only requires an overpotential of 63 mV, far lower than that of the NiS (218 mV), TiS_{2-x} -NF (251 mV) and TiS_2 -NF (314 mV) catalysts. When 0.5 M H_2SO_4 solution is used, an overpotential of 134 mV is needed for the $\text{TiS}_{2-x}/\text{NiS}$ catalyst to achieve a current density of -10 mA cm^{-2} , much smaller than that of the NiS (272 mV), TiS_{2-x} -NF (368 mV) and TiS_2 -NF (382 mV) catalysts. More importantly, the overpotentials for the $\text{TiS}_{2-x}/\text{NiS}$ electrocatalyst to obtain a current density of -100 mA cm^{-2} just need 179 and 288 mV in 1.0 M KOH and 0.5 M H_2SO_4 solutions, respectively. Comparing these HER performances of $\text{TiS}_{2-x}/\text{NiS}$ electrocatalyst in alkaline and acid media, it is intuitive that this electrocatalyst is more capable to dissociate water, promoting the following hydrogen adsorption and recombination, bringing with prominently boosted HER kinetics in alkaline medium. Furthermore, the HER performance offered by this $\text{TiS}_{2-x}/\text{NiS}$ catalyst outperforms that of the recently reported titanium sulfide or nickel sulfide-based catalysts (Fig. 4f) in both acidic [17,43–46] and alkaline media [18,19,47–51] under identified conditions. The recently reported metal sulfide based electrocatalyst are listed in Table S4, including WS_2 , MoS_2 , TaS_2 , NbS_2 , FeS_2 and ReS_2 etc. Making a comparison of their HER performances to that of $\text{TiS}_{2-x}/\text{NiS}$ catalyst, it turns

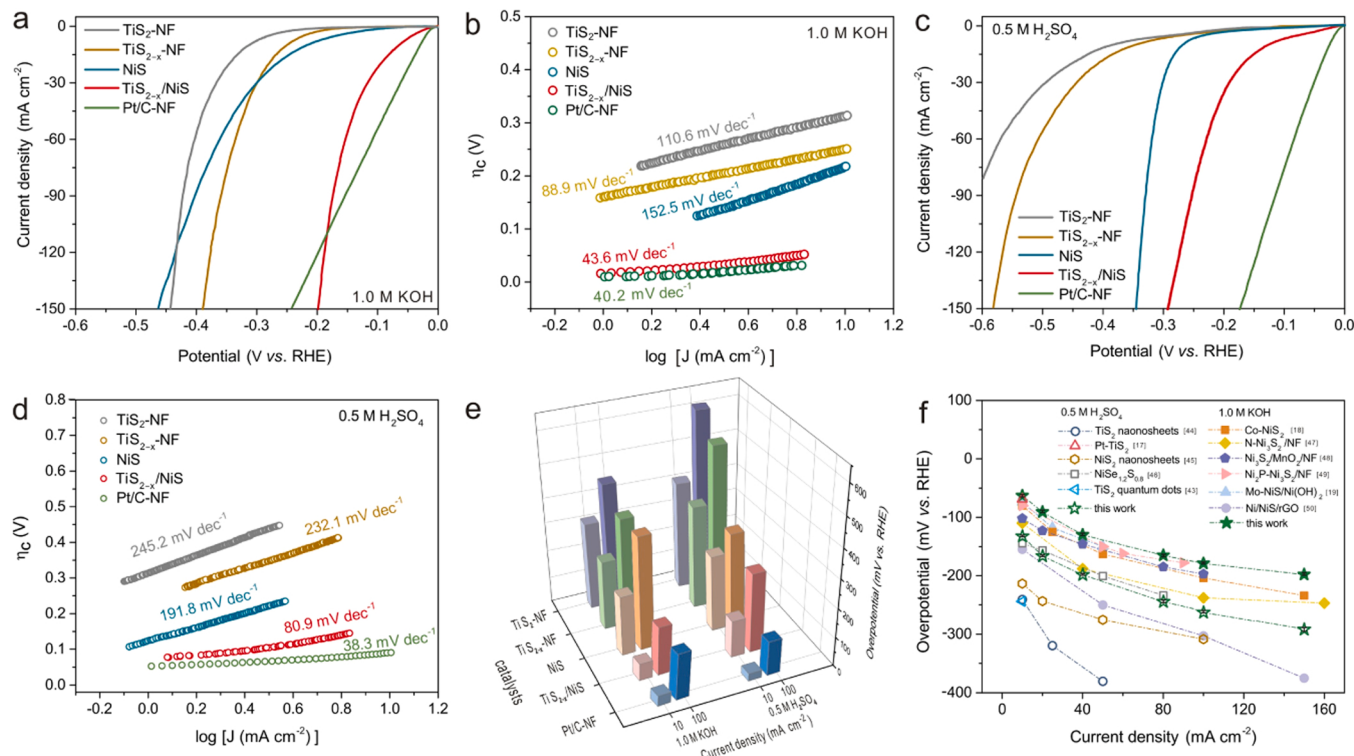


Fig. 4. HER performances of the TiS_{2-x}/NiS catalyst in acidic and alkaline media: (a) The *iR*-corrected HER polarization curves of the TiS₂-NF, TiS_{2-x}-NF, NiS, TiS_{2-x}/NiS and Pt/C-NF catalysts in 1.0 M KOH solution; (b) Tafel plots for these catalysts; (c) The *iR*-corrected HER polarization curves of these catalysts in 0.5 M H₂SO₄; (d) Tafel plots for these catalysts; (e) Comparison of HER overpotentials on these catalysts at a current density of 10 mA cm⁻² and 100 mA cm⁻² in both media; (f) Comparison of the overpotential on the TiS_{2-x}/NiS catalyst to harvest a current density of 10 or 100 mA cm⁻² with that on the reported electrocatalysts in both acidic [17,43–46] and alkaline media. [18,19,47–51] Error bars reveal the standard deviation calculated from at least three experimental repeats on different batches of TiS_{2-x}/NiS catalysts.

out that TiS_{2-x}/NiS catalyst exerting glorious HER activities locates at the leading level and exceeds most of the metal sulfide based electrocatalyst. Notably, at least three different batches of obtained TiS_{2-x}/NiS catalysts were carried out with the related electrochemical experiments, the relatively narrow error bars in Fig. 4f reveal the reproducibility of this work. Additionally, the turn over frequency (TOF) values of TiS_{2-x}/NiS catalyst at -0.15 V vs. RHE were calculated to be 0.81 and $0.26 \text{ H}_2 \text{ S}^{-1}$ in 1 M KOH and 0.5 M H₂SO₄, respectively. Consequently, the TiS_{2-x}/NiS catalyst does exhibit outstanding HER performance in both alkaline and acid media.

Since the surface area of an electrocatalyst affects dramatically on its HER performance, the electrochemical surface areas (ECSA) of the NiS, TiS_{2-x}-NF, TiS₂-NF, TiS_{2-x}/NiS catalysts were estimated by means of cyclic voltammetry in both 1.0 M KOH and 0.5 M H₂SO₄ solutions. From the cyclic voltammograms of the TiS_{2-x}/NiS (Fig. S21), NiS (Fig. S22), TiS_{2-x}-NF (Fig. S23), and TiS₂-NF (Fig. S24) catalysts recorded at different scan rates, their double-layer capacitances (C_{dl}) were estimated. The TiS_{2-x}/NiS catalyst has the largest C_{dl} values (e.g., 11.01 mF cm⁻² in 1.0 M KOH and 12.98 mF cm⁻² in 0.5 M H₂SO₄) in Fig. S25, suggesting its largest ECSA and R_f value (Table S5). The ECSA-normalized LSVs (Fig. S26) reveal again that the overpotential of the TiS_{2-x}/NiS catalyst is lower than that of the other tested catalysts under an identical current density. Furthermore, the BET measurements were operated to calculate the specific surface areas (SSAs) of these catalysts (Fig. S27). The variation tendency of their SSAs agrees well with their ECSA. In more detail, the TiS_{2-x}/NiS catalyst possesses a SSA of $10.19 \text{ m}^2 \text{ g}^{-1}$, larger than that of the NiS ($6.11 \text{ m}^2 \text{ g}^{-1}$), TiS_{2-x}-NF ($3.85 \text{ m}^2 \text{ g}^{-1}$) and TiS₂-NF ($3.22 \text{ m}^2 \text{ g}^{-1}$) catalysts. The TiS_{2-x}/NiS catalyst is thus endowed with affluent and potential reactive sites for the HER. Hence, it can be conjectured that the inherent catalytic activity offered by the TiS_{2-x}/NiS heterointerface brings up the splendid HER

performance in both acidic and alkaline media. To further testify this statement, the charge transfer resistance of the TiS_{2-x}/NiS catalyst was estimated from its Nyquist plot (Fig. S28). As expected, it is smaller than that of the NiS, TiS₂-NF or TiS_{2-x}-NF catalysts. In addition, gas chromatography was utilized to analyze the amounts of H₂ generated at various potentials. An almost 100% Faradaic efficiency was obtained on the TiS_{2-x}/NiS catalyst toward both alkaline and acidic HER (Fig. S29).

The chronoamperometry and the accelerated degradation tests (ADTs) were then executed to evaluate the durability of the TiS_{2-x}/NiS catalyst. Both alkaline and acidic HER polarization curves of the TiS_{2-x}/NiS catalyst exhibit undiminished catalytic activity even after 1000 cycles of reduplicative CVs (Fig. S30). Meanwhile, the long-time durability tests of 100 h were conducted (Fig. S31), where no obvious changes are seen in the recorded curves of chronoamperometry during maintaining current densities of 10 mA cm⁻² or 100 mA cm⁻². Even at a high current density of 500 mA cm⁻² (Fig. S32), TiS_{2-x}/NiS catalyst still exhibited reliable stability which could be qualified as a promising candidate for the superior HER catalysts application in the future. These results confirm again the robust durability of the TiS_{2-x}/NiS catalyst toward the HER in both alkaline and acidic solutions. To figure out the reasons of such high stability of the TiS_{2-x}/NiS catalyst, the characterization of used TiS_{2-x}/NiS catalyst after these stability tests were performed. A well-maintained morphology and crystal structure of the TiS_{2-x}/NiS catalyst is noticed from the SEM and TEM images of the TiS_{2-x}/NiS catalyst after such a durability test (Fig. S33). The EPR spectra of the TiS_{2-x}/NiS catalyst (Fig. S34) after this durability test in 1.0 M KOH and 0.5 M H₂SO₄ reveal the density of S-vacancies barely changed by contrast to that before test. The stable existence of S-vacancies during the whole HER process could be one of the reason for the outstanding durability of TiS_{2-x}/NiS catalyst. For one thing, S-vacancies could boost the catalytic activity of TiS_{2-x}/NiS catalyst via regulating

the coordination environment of adjacent Ti or Ni atoms to endow them with low coordination, then possessing high intrinsic electrocatalytic activity. For another thing, when Ti and Ni atoms serve as active sites, S vacancies could induce S atoms to provide sites for hydrogen to adsorb and desorb, thereby accelerating the reaction kinetics. The XRD patterns (Fig. S35) and XPS spectra (Fig. S36) of the $\text{TiS}_{2-x}/\text{NiS}$ catalyst after this durability test remain unchanged chemical composition and elemental states, respectively. Among them, only the element valence of S atoms changed slightly, giving the possibility of S atoms in providing sites for desorption/adsorption of hydrogen for HER process. These results verify the superior stability of the $\text{TiS}_{2-x}/\text{NiS}$ catalyst towards the HER in both alkaline and acidic media.

3.3. DFT calculations

When the Volmer reaction, Heyrovsky reaction, or Tafel reaction are the rate-determining step of HER, the corresponding Tafel slopes should be around 120, 40, or 30 mV dec⁻¹, respectively [52]. According to the DFT computation results and as-obtained Tafel values (43.6 dec⁻¹ in 1.0 M KOH and 80.9 dec⁻¹ in 0.5 M H₂SO₄) on the $\text{TiS}_{2-x}/\text{NiS}$ catalyst toward the HER, the HER mechanism on the two circumstances is assumed as a Volmer–Heyrovsky route [53]. To get a better understanding of this mechanism and excavate the interrelation between electronic structure of this catalyst and its illustrious HER activity, the dynamics energy barriers of both a Volmer step and a Heyrovsky step

were calculated, where a model of $\text{TiS}_{2-x}/\text{NiS}$ catalyst is applied. To identify real active sites on this model catalyst, the $\Delta G_{\text{H}_2\text{O}}$ and ΔG_{H^*} of all sites were calculated. The corresponding adsorption configurations for HER on NiS side (Fig. S37), TiS_{2-x} side (Fig. S38), and $\text{TiS}_{2-x}/\text{NiS}$ heterointerface (Fig. S39) of the $\text{TiS}_{2-x}/\text{NiS}$ catalyst in alkaline and acidic solutions were supplied. In an alkaline electrolyte, H_2O dissociation occurs on a Ti site (Fig. 5a), leading to the formation of an adsorbed hydrogen (H^*) by a Volmer step in the form of $\text{H}_2\text{O} + \text{e}^- \rightarrow \text{H}^* + \text{OH}^-$. The energy barrier of this step on the $\text{TiS}_{2-x}/\text{NiS}$ heterointerface is 0.599 eV (Fig. 5b), remarkably smaller than that (0.653 eV) of a TiS_{2-x} side or that (0.741 eV) of a NiS side of the $\text{TiS}_{2-x}/\text{NiS}$ catalyst. Subsequently, the as-obtained H^* incorporates with an electron (e^-) and a H_2O molecule to generate a H_2 molecule, following a Heyrovsky step in the form of $\text{H}^* + \text{H}_2\text{O} + \text{e}^- \rightarrow \text{OH}^- + \text{H}_2$. Similarly, the ΔG_{H^*} on the $\text{TiS}_{2-x}/\text{NiS}$ heterointerface is 0.137 eV, which is lower than that (0.223 eV) of a TiS_{2-x} side or that (0.314 eV) of a NiS side on the $\text{TiS}_{2-x}/\text{NiS}$ catalyst.

Unlike what occurs in alkaline media, the protons (H^+) are participated in the HER catalytic reaction in acidic solution on the $\text{TiS}_{2-x}/\text{NiS}$ catalyst (Fig. 5c). The emergence of H^* is generated by adsorbing H^+ on a Ti site, namely via the proceeding of a Volmer step. The ΔG_{H^*} on the $\text{TiS}_{2-x}/\text{NiS}$ heterointerface is thus lower than that on the TiS_{2-x} side or the NiS side of the $\text{TiS}_{2-x}/\text{NiS}$ catalyst (Fig. 5d). Subsequently, the as-gained H^* combines with an electron and a proton to generate a H_2 via a Heyrovsky step. Overall, the DFT calculation results reveal that the

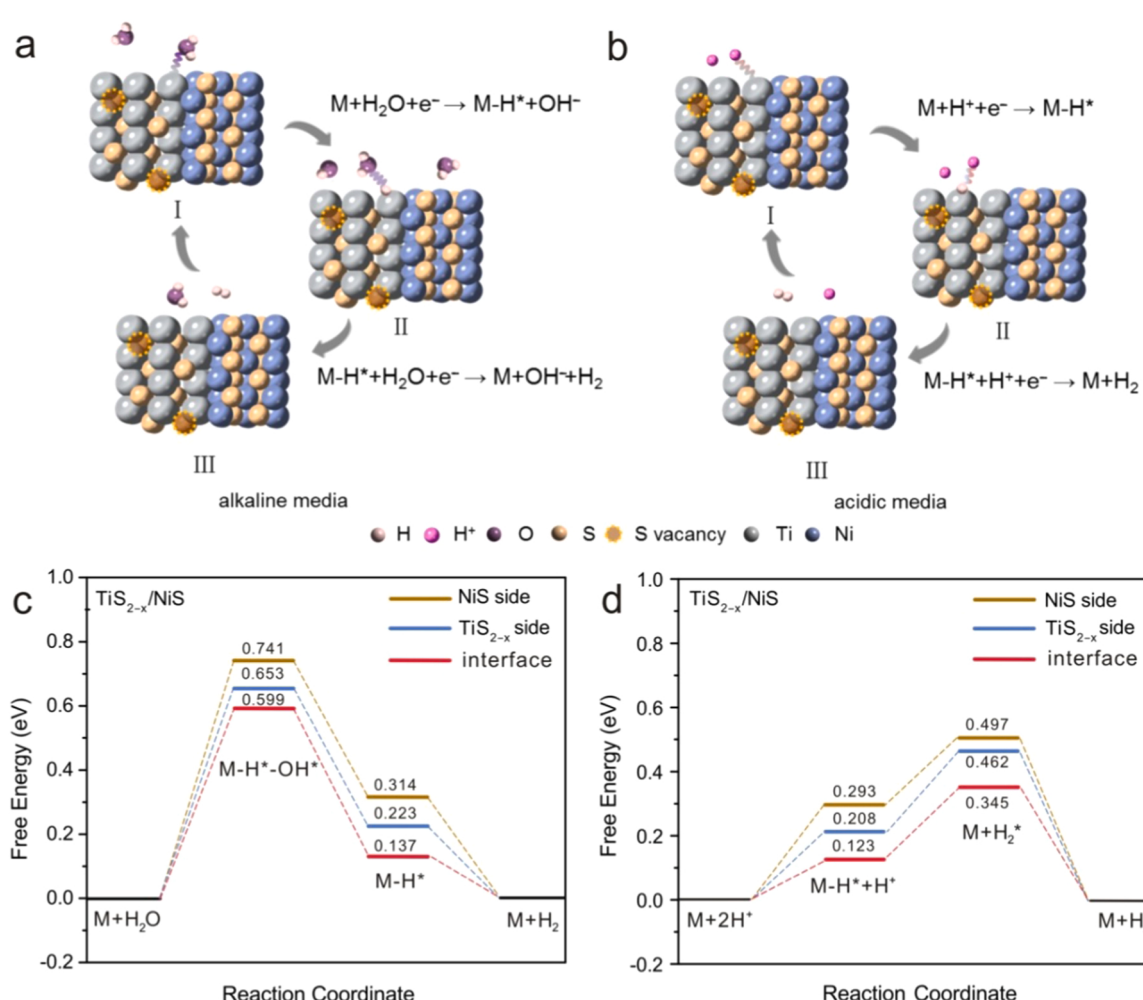


Fig. 5. Mechanisms of the $\text{TiS}_{2-x}/\text{NiS}$ catalyst for boosted HER: Schematics for the proposed HER pathways on the $\text{TiS}_{2-x}/\text{NiS}$ catalyst in (a) alkaline and (b) acidic media; The corresponding free energy diagrams of the $\text{TiS}_{2-x}/\text{NiS}$ catalyst for (c) alkaline and (d) acidic HER on the TiS_{2-x} side, the NiS side, and the $\text{TiS}_{2-x}/\text{NiS}$ heterointerface.

introduction of the S-vacancies into the $\text{TiS}_{2-x}/\text{NiS}$ heterointerface lowers the energy barrier of both Volmer and Heyrovsky steps, concurrently optimizes the $\text{TiS}_{2-x}/\text{NiS}$ catalyst for the HER in both alkaline and acidic media.

4. Conclusion

A nonstoichiometric $\text{TiS}_{2-x}/\text{NiS}$ heterostructure has been constructed. Since this $\text{TiS}_{2-x}/\text{NiS}$ heterostructure possesses abundant sulfur vacancies, as verified by X-ray photoelectron spectroscopy, electron paramagnetic resonance and X-ray absorption fine structure analysis, it has been employed as the HER catalyst, where high HER performance is realized in both alkaline and acidic media. Experimental results and theoretical calculations confirm that such a nonstoichiometric $\text{TiS}_{2-x}/\text{NiS}$ heterostructure accompanied by abundant sulfur vacancies or multiple active sites effectively regulates the *d*-electronic structure of metal Ti and Ni atoms. Consequently, the adsorption energy of H^* is optimized in both alkaline and acidic media and the HER kinetics is boosted on this $\text{TiS}_{2-x}/\text{NiS}$ catalyst. Future work can be conducted on the effect of the composition and morphology of used metal sulfides on their HER performance in both alkaline and acidic media. In summary, this work provides the guidance in applying a nonstoichiometric effect for the modulation of electronic structure of a HER electrocatalyst and further in exploring the applications of such catalysts for high-efficient water electrolysis.

Author contributions section

The conceptualization and methodology of the experiment were offered by Jing Wu and Wenda Zhong and Chenfan Yang. Rong Zhao and Wenli Xu and Hui Xiang carried out measurements. Qin Zhang and Xuanke Li and Nianjun Yang analyzed experimental and computational results. The manuscript was written with contributions from all authors.

CRediT authorship contribution statement

Conceptualization: Q. Zhang, X. Li, N. Yang **Methodology:** J. Wu, W. zhong, C. Yang, W. Xu, R. Zhao **Investigation:** J. Wu, W. zhong, C. Yang, W. Xu, R. Zhao **Writing – Original draft:** J. Wu, W. zhong, C. Yang, W. Xu, R. Zhao **Writing – Review & Editing:** Q. Zhang, N. Yang **Supervision:** H. Xiang, Q. Zhang, X. Li, N. Yang **Project administration:** Q. Zhang, X. Li **Funding acquisition:** Q. Zhang, X. Li.

Declaration of Competing Interest

The authors declare that they have no known competing financial interests or personal relationships that could have appeared to influence the work reported in this paper.

Acknowledgements

The research was supported by the National Natural Science Foundation of China (Grants No. U1864207 and 51902232).

Appendix A. Supporting information

Supplementary data associated with this article can be found in the online version at [doi:10.1016/j.apcatb.2022.121332](https://doi.org/10.1016/j.apcatb.2022.121332).

References

- [1] S. van Renssen, The hydrogen solution? *Nat. Clim. Change* 10 (2020) 799–801, <https://doi.org/10.1038/s41558-020-0891-0>.
- [2] A Clean Planet for all: A European Long-term Strategic Vision for a Prosperous, Modern, Competitive and Climate Neutral Economy (European Commission, 2018).
- [3] The Future of Hydrogen (IEA, 2019).
- [4] J. Töpler, J. Lehmann, *Hydrogen and fuel cell: technologies and market perspectives*, Springer-Verlag, 2014.
- [5] L. An, J. Feng, Y. Zhang, R. Wang, H. Liu, G.-C. Wang, F. Cheng, P. Xi, Epitaxial heterogeneous interfaces on N-NiMoO₄/NiS₂ nanowires/nanosheets to boost hydrogen and oxygen production for overall water splitting, *Adv. Funct. Mater.* 29 (2019), 1805298, <https://doi.org/10.1002/adfm.201805298>.
- [6] J. Chen, M. Qin, S. Ma, R. Fan, X. Zheng, S. Mao, C. Chen, Y. Wang, Rational construction of Pt/PtTex interface with optimal intermediate adsorption energy for efficient hydrogen evolution reaction, *Appl. Catal. B Environ.* 299 (2021), 120640, <https://doi.org/10.1016/j.apcatb.2021.120640>.
- [7] J. Wu, Q. Zhang, K. Shen, R. Zhao, W. Zhong, C. Yang, H. Xiang, X. Li, N. Yang, Modulating interband energy separation of boron-doped Fe₇S₈/FeS₂ electrocatalysts to boost alkaline hydrogen evolution reaction, *Adv. Funct. Mater.* 30 (2021), 2107802, <https://doi.org/10.1002/adfm.202107802>.
- [8] J. Yin, Y. Li, F. Lv, Q. Fan, Y.-Q. Zhao, Q. Zhang, W. Wang, F. Cheng, P. Xi, S. Guo, NiO/Co porous nanowires as efficient bifunctional catalysts for Zn-air batteries, *ACS Nano* 11 (2017) 2275–2283, <https://doi.org/10.1021/acsnano.7b00417>.
- [9] L. Wang, Z. Li, K. Wang, Q. Dai, C. Lei, B. Yang, Q. Zhang, L. Lei, M.K.H. Leung, Y. Hou, Tuning d-band center of tungsten carbide via Mo doping for efficient hydrogen evolution and Zn-H₂O cell over a wide pH range, *Nano Energy* 74 (2020), 104850, <https://doi.org/10.1016/j.nanoen.2020.104850>.
- [10] H. Jang, W. Jin, G. Nam, Y. Yoo, J.S. Jeon, J. Park, M.G. Kim, J. Cho, Exploring the artificially induced nonstoichiometric effect of Li₂RuO₃ as a reactive promoter on electrocatalytic behavior, *Energy Environ. Sci.* 13 (2020) 2167–2177, <https://doi.org/10.1039/d0ee00859a>.
- [11] D. Zhang, Y. Shi, H. Zhao, W. Qi, X. Chen, T. Zhan, S. Li, B. Yang, M. Sun, J. Lai, B. Huang, L. Wang, The facile oil-phase synthesis of a multi-site synergistic high-entropy alloy to promote the alkaline hydrogen evolution reaction, *J. Mater. Chem. A* 9 (2021) 889–893, <https://doi.org/10.1039/d0ta10574k>.
- [12] Z. Jia, K. Nomoto, Q. Wang, C. Kong, L. Sun, L.C. Zhang, S.X. Liang, J. Lu, J. J. Kružić, A self-supported high-entropy metallic glass with a nanospunge architecture for efficient hydrogen evolution under alkaline and acidic conditions, *Adv. Funct. Mater.* 31 (2021), 2101586, <https://doi.org/10.1002/adfm.202101586>.
- [13] L.-C. Zhang, Z. Jia, F. Lyu, S.-X. Liang, J. Lu, A review of catalytic performance of metallic glasses in wastewater treatment: recent progress and prospects, *Prog. Mater. Sci.* 105 (2019), 100576, <https://doi.org/10.1016/j.pmatsci.2019.100576>.
- [14] X. Mu, J. Gu, F. Feng, Z. Xiao, C. Chen, S. Liu, S. Mu, RuRh bimetallic nanorings as high-efficiency ph-universal catalyst for hydrogen evolution reaction, *Adv. Sci.* 8 (2020), 2002341, <https://doi.org/10.1002/advs.202002341>.
- [15] X. Liu, L. Yang, Z. Zhou, L. Zeng, H. Liu, Y. Deng, J. Yu, C. Yang, W. Zhou, N doped carbon coated multi-metals nanoparticles decorated perovskite as electrocatalyst for efficient hydrogen evolution reaction, *Chem. Eng. J.* 399 (2020), 125779, <https://doi.org/10.1016/j.cej.2020.125779>.
- [16] Z. Jia, T. Yang, L. Sun, Y. Zhao, W. Li, J. Luan, F. Lyu, L.C. Zhang, J.J. Kružić, J. J. Kai, J.C. Huang, J. Lu, C.T. Liu, A novel multinary intermetallic as an active electrocatalyst for hydrogen evolution, *Adv. Mater.* 32 (2020), 2000385, <https://doi.org/10.1002/adma.202000385>.
- [17] Z. Zeng, C. Tan, X. Huang, S. Bao, H. Zhang, Growth of noble metal nanoparticles on single-layer TiS₂ and TaS₂ nanosheets for hydrogen evolution reaction, *Energy Environ. Sci.* 7 (2014) 797–803, <https://doi.org/10.1039/C3EE42620C>.
- [18] J. Yin, J. Jin, H. Zhang, M. Lu, Y. Peng, B. Huang, P. Xi, C.H. Yan, Atomic arrangement in metal-doped NiS₂ boosts the hydrogen evolution reaction in alkaline media, *Angew. Chem. Int. Ed. Engl.* 131 (2019) 18849–18855, <https://doi.org/10.1002/ange.201911470>.
- [19] H. Zhang, B. Xi, Y. Gu, W. Chen, S. Xiong, Interface engineering and heterometal doping Mo-NiS/Ni(OH)₂ for overall water splitting, *Nano Res.* 14 (2021) 3466–3473, <https://doi.org/10.1007/s12274-021-3557-y>.
- [20] J. Sun, W. Xu, C. Lv, L. Zhang, M. Shakouri, Y. Peng, Q. Wang, X. Yang, D. Yuan, M. Huang, Y. Hu, D. Yang, L. Zhang, Co/MoN hetero-interface nanoflake array with enhanced water dissociation capability achieves the Pt-like hydrogen evolution catalytic performance, *Appl. Catal. B Environ.* 286 (2021), 119882, <https://doi.org/10.1016/j.apcatb.2021.119882>.
- [21] J. Kibsgaard, C. Tsai, K. Chan, J.D. Benck, J.K. Nørskov, F. Abild-Pedersen, T. F. Jaramillo, Designing an improved transition metal phosphide catalyst for hydrogen evolution using experimental and theoretical trends, *Energy Environ. Sci.* 8 (2015) 3022–3029, <https://doi.org/10.1039/C5ee02179k>.
- [22] L. Li, Z. Qin, L. Ries, S. Hong, T. Michel, J. Yang, C. Salameh, M. Bechelany, P. Miele, D. Kaplan, M. Chhowalla, D. Voiry, Role of sulfur vacancies and undercoordinated Mo regions in MoS₂ nanosheets toward the evolution of hydrogen, *ACS Nano* 13 (2019) 6824–6834, <https://doi.org/10.1021/acsnano.9b01583>.
- [23] P. Sabhapathy, I. Shown, A. Sabbah, P. Raghunath, J.-L. Chen, W.-F. Chen, M.-C. Lin, K.-H. Chen, L.-C. Chen, Electronic structure modulation of isolated Co-N₄ electrocatalyst by sulfur for improved pH-universal hydrogen evolution reaction, *Nano Energy* 80 (2021), 105544, <https://doi.org/10.1016/j.nanoen.2020.105544>.
- [24] P. Sabhapathy, C.-C. Liao, W.-F. Chen, T.-C. Chou, I. Shown, A. Sabbah, Y.-G. Lin, J.-F. Lee, M.-K. Tsai, K.-H. Chen, L.-C. Chen, Highly efficient nitrogen and carbon coordinated N-Co-C electrocatalysts on reduced graphene oxide derived from vitamin-B12 for the hydrogen evolution reaction, *J. Mater. Chem. A* 7 (2019) 7179–7185, <https://doi.org/10.1039/c8ta10935d>.
- [25] S. Fang, X. Zhu, X. Liu, J. Gu, W. Liu, D. Wang, W. Zhang, Y. Lin, J. Lu, S. Wei, Y. Li, T. Yao, Uncovering near-free platinum single-atom dynamics during electrochemical hydrogen evolution reaction, *Nat. Commun.* 11 (2020) 1029, <https://doi.org/10.1038/s41467-020-14848-2>.

- [26] B. Qin, Y. Li, H. Wang, G. Yang, Y. Cao, H. Yu, Q. Zhang, H. Liang, F. Peng, Efficient electrochemical reduction of CO₂ into CO promoted by sulfur vacancies, *Nano Energy* 60 (2019) 43–51, <https://doi.org/10.1016/j.nanoen.2019.03.024>.
- [27] V. Vega-Mayoral, R. Tian, A.G. Kelly, A. Griffin, A. Harvey, M. Borrelli, K. Nisi, C. Backes, J.N. Coleman, Solvent exfoliation stabilizes TiS₂ nanosheets against oxidation, facilitating lithium storage applications, *Nanoscale* 11 (2019) 6206–6216, <https://doi.org/10.1039/c8nr09446b>.
- [28] J. Kang, L.-W. Wang, Robust band gap of TiS₃ nanofilms, *Phys. Chem. Chem. Phys.* 18 (2016) 14805–14809, <https://doi.org/10.1039/C6CP01125J>.
- [29] I.M. Lifshitz, A.M. Kosevich, The dynamics of a crystal lattice with defects, *Rep. Prog. Phys.* 29 (1966) 217–254, <https://doi.org/10.1088/0034-4885/29/1/305>.
- [30] J. Wang, Y. Chen, W. Zhou, G. Tian, Y. Xiao, H. Fu, H. Fu, Cubic quantum dot/hexagonal microsphere ZnIn₂S₄ heterophase junctions for exceptional visible-light-driven photocatalytic H₂ evolution, *J. Mater. Chem. A* 5 (2017) 8451–8460, <https://doi.org/10.1039/C7TA01914A>.
- [31] H. Tao, M. Zhou, R. Wang, K. Wang, S. Cheng, K. Jiang, TiS₂ as an advanced conversion electrode for sodium-ion batteries with ultra-high capacity and long-cycle life, *Adv. Sci.* 5 (2018), 1801021, <https://doi.org/10.1002/advs.201801021>.
- [32] B. Guan, Y. Li, B. Yin, K. Liu, D. Wang, H. Zhang, C. Cheng, Synthesis of hierarchical NiS microflowers for high performance asymmetric supercapacitor, *Chem. Eng. J.* 308 (2017) 1165–1173, <https://doi.org/10.1016/j.cej.2016.10.016>.
- [33] S. Yu, N. Yang, H. Zhuang, S. Mandal, O.A. Williams, B. Yang, N. Huang, X. Jiang, Battery-like supercapacitors from diamond networks and water-soluble redox electrolytes, *J. Mater. Chem. A* 5 (2017) 1778–1785, <https://doi.org/10.1039/c6ta08607a>.
- [34] J.C. Dupina, D. Gonbeaua, I. Martin-Litasb, P. Vinatierb, A. Levasseur, Amorphous oxysulfide thin films Mo_xS₂ (M = W, Mo, Ti) XPS characterization: structural and electronic peculiarities, *Appl. Surf. Sci.* 173 (2001) 140–150, [https://doi.org/10.1016/S0169-4332\(00\)00893-X](https://doi.org/10.1016/S0169-4332(00)00893-X).
- [35] P. Wang, X. Zhang, J. Zhang, S. Wan, S. Guo, G. Lu, J. Yao, X. Huang, Precise tuning in platinum-nickel/nickel sulfide interface nanowires for synergistic hydrogen evolution catalysis, *Nat. Commun.* 8 (2017) 14580, <https://doi.org/10.1038/ncomms14580>.
- [36] M.E. Fleet, S.L. Harmer, X. Liu, H.W. Nesbitt, Polarized X-ray absorption spectroscopy and XPS of TiS₃: S K- and Ti L-edge XANES and S and Ti 2p XPS, *Surf. Sci.* 584 (2005) 133–145, <https://doi.org/10.1016/j.susc.2005.03.048>.
- [37] K. Taniguchi, Y. Gu, Y. Katsura, T. Yoshino, H. Takagi, Rechargeable Mg battery cathode TiS₃ with d-p orbital hybridized electronic structures, *Appl. Phys. Express* 9 (2016), 011801, <https://doi.org/10.7567/APEX.9.011801>.
- [38] L. Zhang, D. Sun, J. Kang, H.-T. Wang, S.-H. Hsieh, W.-F. Pong, H.A. Bechtel, J. Feng, L.-W. Wang, E.J. Cairns, J. Guo, Tracking the chemical and structural evolution of the TiS₂ electrode in the lithium-ion cell using operando X-ray absorption spectroscopy, *Nano Lett.* 18 (2018) 4506–4515, <https://doi.org/10.1021/acs.nanolett.8b01680>.
- [39] Z.Y. Wu, G. Ouvrard, P. Moreau, C.R. Natoli, Interpretation of preedge features in the Ti and S K-edge x-ray-absorption near-edge spectra in the layered disulfides TiS₂ and TaS₂, *Phys. Rev. B* 55 (1997) 9508–9513, <https://doi.org/10.1103/PhysRevB.55.9508>.
- [40] P.Y. Raval, N.P. Joshi, P.R. Pansara, N.H. Vasoya, S. Kumar, S.N. Dolia, K.B. Modi, R.K. Singh, A Ti L3,2 - and K-edge XANES and EXAFS study on Fe³⁺ - substituted CaCu₃Ti₄O₁₂, *Ceram. Int.* 44 (2018) 20716–20722, <https://doi.org/10.1016/j.ceramint.2018.08.066>.
- [41] Y. Wu, L. Fan, Q. Liu, S. Chen, W. Huang, F. Chen, G. Liao, C. Zou, Z. Wu, Decoupling the lattice distortion and charge doping effects on the phase transition behavior of VO₂ by titanium (Ti⁴⁺) doping, *Sci. Rep.* 5 (2015) 9328, <https://doi.org/10.1038/srep09328>.
- [42] M.-P. Jiang, K.-K. Huang, J.-H. Liu, D. Wang, Y. Wang, X. Wang, Z.-D. Li, X.-Y. Wang, Z.-B. Geng, X.-Y. Hou, S.-H. Feng, Magnetic-field-regulated TiO₂ {100} facets: a strategy for C-C coupling in CO₂ photocatalytic conversion, *Chem* 6 (2020) 2335–2346, <https://doi.org/10.1016/j.chempr.2020.06.033>.
- [43] Y. Liu, C. Liang, J. Wu, T. Sharifi, H. Xu, Y. Nakaniishi, Y. Yang, C.F. Woellne, A. Aliyan, A.A. Martí, B. Xie, R. Vajtai, W. Yang, P.M. Ajayan, Atomic layered titanium sulfide quantum dots as electrocatalysts for enhanced hydrogen evolution reaction, *Adv. Mater. Interfaces* 5 (2017), 1700895, <https://doi.org/10.1002/admi.201700895>.
- [44] T.P. Nguyen, S. Choi, J.-M. Jeon, K.C. Kwon, H.W. Jang, S.Y. Kim, Transition metal disulfide nanosheets synthesized by facile sonication method for the hydrogen evolution reaction, *J. Phys. Chem. C* 120 (2016) 3929–3935, <https://doi.org/10.1021/acs.jpcc.5b12164>.
- [45] Y. Ge, S.-P. Gao, P. Dong, R. Baines, P.M. Ajayan, M. Ye, J. Shen, Insight into the hydrogen evolution reaction of nickel dichalcogenide nanosheets: activities related to non-metal ligands, *Nanoscale* 9 (2017) 5538–5544, <https://doi.org/10.1039/CN90977G>.
- [46] J. Sun, X. Hu, Z. Huang, T. Huang, X. Wang, H. Guo, F. Dai, D. Sun, Atomically thin defect-rich Ni-Se-S hybrid nanosheets as hydrogen evolution reaction electrocatalysts, *Nano Res.* 13 (2020) 2056–2062, <https://doi.org/10.1007/s12274-020-2807-8>.
- [47] P. Chen, T. Zhou, M. Zhang, Y. Tong, C. Zhong, N. Zhang, L. Zhang, C. Wu, Y. Xie, 3D nitrogen-anion-decorated nickel sulfides for highly efficient overall water splitting, *Adv. Mater.* 29 (2017), 1701584, <https://doi.org/10.1002/adma.201701584>.
- [48] Y. Xiong, L. Xu, C. Jin, Q. Sun, Interface-engineered atomically thin Ni₃S₂/MnO₂ heterogeneous nanoarrays for efficient overall water splitting in alkaline media, *Appl. Catal. B Environ.* 254 (2019) 329–338, <https://doi.org/10.1016/j.apcatb.2019.05.017>.
- [49] L. Zeng, K. Sun, X. Wang, Y. Liu, Y. Pan, Z. Liu, D. Cao, Y. Song, S. Liu, C. Liu, Three-dimensional-networked Ni₂P/Ni₃S₂ heteronanoflake arrays for highly enhanced electrochemical overall-water-splitting activity, *Nano Energy* 51 (2018) 26–36, <https://doi.org/10.1016/j.nanoen.2018.06.048>.
- [50] M.B.Z. Hegazy, M.R. Berber, Y. Yamauchi, A. Pakdel, R. Cao, U.-P. Apfel, Synergistic electrocatalytic hydrogen evolution in Ni/NiS nanoparticles wrapped in multi-heteroatom-doped reduced graphene oxide nanosheets, *ACS Appl. Mater. Inter.* 13 (2021) 34043–34052, <https://doi.org/10.1021/acsami.1c05888>.
- [51] C. Li, M. Liu, H. Ding, L. He, E. Wang, B. Wang, S. Fan, K. Liu, A lightly Fe-doped (Ni₃S₂/MoS₂)/carbon nanotube hybrid electrocatalyst film with laser-drilled micropores for stabilized overall water splitting and pH-universal hydrogen evolution reaction, *J. Mater. Chem. A* 8 (2020) 17527–17536, <https://doi.org/10.1039/DOTA04586A>.
- [52] L. Zhang, Y. Zheng, J. Wang, Y. Geng, B. Zhang, J. He, J. Xue, T. Frauenheim, M. Li, Ni/Mo bimetallic-oxide-derived heterointerface-rich sulfide nanosheets with Co-doping for efficient alkaline hydrogen evolution by boosting volmer reaction, *Small* 17 (2021), 2006730, <https://doi.org/10.1002/smll.202006730>.
- [53] J. Wu, R. Zhao, H. Xiang, C. Yang, W. Zhong, C. Zhang, Q. Zhang, X. Li, N. Yang, Exposing highly active (100) facet on a SnS₂/SnO₂ electrocatalyst to boost efficient hydrogen evolution, *Appl. Catal. B Environ.* 292 (2021), 120200, <https://doi.org/10.1016/j.apcatb.2021.120200>.